Geophys. J. Int. (2000) **141,** 175–203

Fréchet kernels for finite-frequency traveltimes—II. Examples

S.-H. Hung, F. A. Dahlen and Guust Nolet

Department of Geosciences, Princeton University, Princeton, NJ 08544, *USA. E-mail: shung@princeton.edu*

Accepted 1999 November 9. Received 1999 November 5; in original form 1999 May 14

SUMMARY

3-D Born–Fréchet traveltime kernel theory is recast in the context of scalar-wave propagation in a smooth acoustic medium, for simplicity. The predictions of the theory are in excellent agreement with 'ground truth' traveltime shifts, measured by cross-correlation of heterogeneous-medium and homogeneous-medium synthetic seismograms, computed using a parallelized pseudospectral code. Scattering, wave-front healing and other finite-frequency diffraction effects can give rise to cross-correlation traveltime shifts that are in significant disagreement with geometrical ray theory, whenever the cross-path width of wave-speed heterogeneity is of the same order as the width of the banana–doughnut Fréchet kernel surrounding the ray. A concentrated off-path slow or fast anomaly can give rise to a larger traveltime shift than one directly on the ray path, by virtue of the hollow-banana character of the kernel. The often intricate 3-D geometry of the sensitivity kernels of P, PP, PcP, PcP_2, PcP_3, ... and $P+pP$ waves is explored, in a series of colourful cross-sections. The geometries of an absolute PP kernel and a differential $PP-P$ kernel are particularly complicated, because of the minimax nature of the surface-reflected PP wave. The kernel for an overlapping $P+pP$ wave from a shallow-focus source has a banana–doughnut character, like that of an isolated P-wave kernel, even when the teleseismic pulse shape is significantly distorted by the depth phase interference. A numerically economical representation of the 3-D traveltime sensitivity, based upon the paraxial approximation, is in excellent agreement with the 'exact' ray-theoretical Fréchet kernel.

Key words: body waves, Fréchet derivatives, global seismology, ray theory, tomography, traveltime.

1 INTRODUCTION

This is the second in a series of two back-to-back papers devoted to the analysis of 3-D Fréchet kernels for finite-frequency seismic traveltimes, measured by cross-correlation of a broad-band waveform with a spherical-earth synthetic seismogram. In the first paper (Dahlen *et al.* 2000, hereafter referred to as Banana–Doughnut I), we used the Born approximation, in conjunction with body wave ray theory, to develop a general procedure for computing such cross-correlation traveltime kernels. In the most general formulation, the Fréchet kernel for a body wave phase of interest is expressed as a double sum over all forward-propagating waves from the source and all backward-propagating waves from the receiver, to every single scatterer in the earth. Upon ignoring all but like-type forward scattering, and introducing the Hessians of the forward and backward traveltime fields, we can approximate this numerically intensive double-sum representation by a compact paraxial expansion, which can be computed extremely economically by implementing a single kinematic and dynamic ray trace along each central source-to-receiver ray.

In the present paper (Banana–Doughnut II), we undertake a more quantitative, visual examination of the effects of scattering, wave-front healing and diffraction upon both seismic waveforms and cross-correlation traveltimes, restricting attention to scalar-wave propagation in an acoustic medium, for reasons of simplicity. We first demonstrate the validity of our Born–Fréchet kernel theory by numerical comparison of the predicted traveltime shifts with 'ground-truth' shifts measured by cross-correlation of a suite of pseudospectral synthetic seismograms. We then present a pictorial glossary of 3-D, differential and absolute traveltime kernels for a number of commonly observed, direct and reflected seismic phases in a simple, smooth, acoustic model of the mantle. The validity of the paraxial approximation is assessed by comparison of a number of paraxial kernels with the full, double-sum formulation.

2 ACOUSTIC WAVE PROPAGATION

All of the results obtained in Banana–Doughnut I are applicable to an acoustic medium; it is simply necessary to set the rigidity μ equal to zero. Many of the complications, which arise

from the proliferation of P, SV, $SH \rightarrow P$, SV, SH polarization interactions at a scatterer, disappear; as a result, all of the double sums over body waves that propagate from the source to a scatterer and then on to the receiver are considerably simplified. To enable the present paper to be easily read without having digested all the grisly details in Banana–Doughnut I, we present an independent derivation of the Fréchet kernels of an acoustic wave traveltime here. The final formulae are identical to those obtained by specialization of the general results to an acoustic medium.

2.1 Equations of motion

We specify the medium in terms of its local density ρ and acoustic wave speed

$$c = \sqrt{\kappa/\rho}\,, \tag{1}$$

where κ is the incompressibility. The linearized equations of motion governing acoustic wave propagation can be written in terms of these two properties in the form

$$\partial_t \mathbf{u} = -\rho^{-1}\nabla p\,, \tag{2}$$

$$\partial_t p = -\rho c^2(\nabla\cdot\mathbf{u}) + \rho c^2 m(t)\delta(\mathbf{r}-\mathbf{s})\,. \tag{3}$$

The unknown quantities $\mathbf{u}$ and p are the velocity of the fluid and the associated incremental pressure at point $\mathbf{r}$ and time t. The final term in (3) represents an assumed source of sound at the point $\mathbf{s}$. We presume that this source is some sort of transient pulse that commences at time $t=0$:

$$m(t) = 0 \quad \text{for } t < 0\,. \tag{4}$$

Physically, $m(t)$ can be regarded as the instantaneous rate of change of an infinitesimally small volume $dV(t)$ situated at the source point $\mathbf{s}$ (Morse & Ingard 1968).

2.2 Infinite homogeneous medium

In an infinite homogeneous medium, with properties

$$\rho = \text{constant}, \quad c = \text{constant}\,, \tag{5}$$

eqs (2) and (3) reduce to the classical wave equation

$$\nabla^2 p - c^{-2}\partial_t^2 p = -\rho\dot{m}(t)\delta(\mathbf{r}-\mathbf{s})\,. \tag{6}$$

Here and elsewhere in this paper, we use a dot to denote differentiation with respect to time. The unique solution to eq. (6) is

$$p(t) = \frac{\rho\dot{m}(t-R/c)}{4\pi R}\,. \tag{7}$$

The quantity $R = \|\mathbf{r}-\mathbf{s}\|$ is the straight-line distance between the source $\mathbf{s}$ and receiver $\mathbf{r}$. The acoustic pressure response (7) is a delayed pulse that propagates with speed c and is geometrically attenuated by a factor R^{-1}. The shape of the pressure pulse is the time derivative of $m(t)$, that is, the second derivative of the differential source volume, $\dot{m}(t) = d\ddot{V}(t)$.

The analogue of eq. (7) in the frequency domain is

$$p(\omega) = \frac{\rho\dot{m}(\omega)\exp(-i\omega R/c)}{4\pi R}\,, \tag{8}$$

where $\dot{m}(\omega)$ is the Fourier transform of the pressure-response pulse $\dot{m}(t)$. Our sign convention is the same as that adopted in Banana–Doughnut I: a factor $\exp(-i\omega t)$ appears in the Fourier integral upon transforming from time t to angular frequency ω.

2.3 Geometrical ray theory

In a smoothly varying heterogeneous medium, the approximate ray-theoretical or JWKB pressure response is a straightforward generalization of the result (8):

$$p(\omega) = \frac{1}{4\pi}\sum_{\text{rays}} (\rho_s\rho_r c_s c_r)^{1/2}(c_s\mathscr{R})^{-1}\dot{m}(\omega) \times \exp i(-\omega T + M\pi/2)\,. \tag{9}$$

The subscripts on ρ_s, c_s and ρ_r, c_r denote evaluation at the source $\mathbf{s}$ and the receiver $\mathbf{r}$, respectively. The summation accounts for the possibility of multipathing, that is, more than one geometrical ray between $\mathbf{s}$ and $\mathbf{r}$. The quantity $T = T_{rs}$ is the traveltime of an acoustic wave along each ray, given by the line integral

$$T = \int_{\mathbf{s}}^{\mathbf{r}} \frac{dl}{c}\,, \tag{10}$$

where dl is the differential arclength. Every passage of a wave through a caustic gives rise to a non-geometrical $\pi/2$ phase shift; the Maslov index $M = M_{rs}$ is a monotonically increasing integer that keeps track of the number of caustic passages and attendant $\pi/2$ phase shifts along each ray. Finally, $\mathscr{R} = \mathscr{R}_{rs}$ is a geometrical attenuation or spreading factor, analogous to the straight-line source–receiver distance $R = \|\mathbf{r}-\mathbf{s}\|$ in a homogeneous medium.

The time-domain response corresponding to (9) is

$$p(t) = \frac{1}{4\pi}\sum_{\text{rays}} (\rho_s\rho_r c_s c_r)^{1/2}(c_s\mathscr{R})^{-1}\dot{m}_H^{(M)}(t-T)\,. \tag{11}$$

Every passage through a caustic acts to Hilbert transform the near-source pressure pulse $\dot{m}(t)$; the M-times-transformed pulse is

$$\dot{m}_H^{(M)}(t) = \frac{1}{\pi}\,\mathscr{R}e\int_0^\infty \dot{m}(\omega)\exp i(\omega t + M\pi/2)\,d\omega\,. \tag{12}$$

The traveltime and number of caustic passages are independent of whether a ray is traced from the source to the receiver or *vice versa*: $T_{rs} = T_{sr}$, $M_{rs} = M_{sr}$. The geometrical spreading factor satisfies a slightly more complicated symmetry relation, namely $c_s\mathscr{R}_{rs} = c_r\mathscr{R}_{sr}$. These kinematic and dynamical symmetries together guarantee that the JWKB responses (9) and (11) are invariant under an interchange of the source and receiver, $\mathbf{s} \leftrightarrow \mathbf{r}$. This is the acoustic version of the principle of source–receiver reciprocity: $p_{sr} = p_{rs}$.

2.4 Born approximation

Suppose now that the properties of the medium are subjected to an infinitesimal perturbation:

$$\rho \rightarrow \rho + \delta\rho\,, \qquad c \rightarrow c + \delta c\,. \tag{13}$$

A straightforward application of the Born approximation yields the resulting first-order frequency-domain pressure

perturbation:

$$\delta p(\omega) = \left(\frac{\omega}{4\pi}\right)^2 \iiint_{\oplus} \left\{ \sum_{\text{rays}'} \sum_{\text{rays}''} (\rho_s \rho_r c_s c_r)^{1/2} \times (c c_s c_r \mathscr{R}' \mathscr{R}'')^{-1} \left[-2\left(\frac{\delta c}{c}\right) - (1 - \hat{\mathbf{k}}' \cdot \hat{\mathbf{k}}'') \left(\frac{\delta \rho}{\rho}\right) \right] \times \dot{m}(\omega) \exp i[-\omega(T' + T'') + (M' + M'')\pi/2] \right\} d^3\mathbf{x} . \quad (14)$$

The integration variable in the representation (14) is the position $\mathbf{x}$ of an arbitrary point scatterer in the region of space $\oplus$ where the perturbations (13) are non-zero. The double sum is over all forward rays$'$ from the source $\mathbf{s}$ and all backward rays$''$ from the receiver $\mathbf{r}$ to the scatterer $\mathbf{x}$; the unit vectors $\hat{\mathbf{k}}'$ and $\hat{\mathbf{k}}''$ are the wave vectors of the incoming and outgoing waves at $\mathbf{x}$, as illustrated in Fig. 1. The other primed and double-primed variables are the traveltimes $T' = T_{xs}$, $T'' = T_{xr}$, the Maslov indices $M' = M_{xs}$, $M'' = M_{xr}$, and the geometrical spreading factors $\mathscr{R}' = \mathscr{R}_{xs}$, $\mathscr{R}'' = \mathscr{R}_{xr}$ along the forward rays$'$ and backward rays$''$.

The equivalent time-domain pressure perturbation is

$$\delta p(t) = -\left(\frac{1}{4\pi}\right)^2 \iiint_{\oplus} \left\{ \sum_{\text{rays}'} \sum_{\text{rays}''} (\rho_s \rho_r c_s c_r)^{1/2} \times (c c_s c_r \mathscr{R}' \mathscr{R}'')^{-1} \left[-2\left(\frac{\delta c}{c}\right) - (1 - \hat{\mathbf{k}}' \cdot \hat{\mathbf{k}}'') \left(\frac{\delta \rho}{\rho}\right) \right] \times \ddot{m}_H^{(M' + M'')}(t - T' - T'') \right\} d^3\mathbf{x} . \quad (15)$$

All of the primed and double-primed quantities in (14) and (15) are invariant under an interchange of the source and receiver, $\mathbf{s} \leftrightarrow \mathbf{r}$, except for the wave vectors, which are reversed: $\hat{\mathbf{k}}' \to -\hat{\mathbf{k}}'$, $\hat{\mathbf{k}}'' \to -\hat{\mathbf{k}}''$. The dot product $\hat{\mathbf{k}}' \cdot \hat{\mathbf{k}}''$ is unaffected by this reversal, however, so that the pressure perturbations $\delta p(\omega)$ and $\delta p(t)$ also satisfy the principle of acoustic source–receiver reciprocity: $\delta p_{sr} = \delta p_{rs}$.

2.5 Acoustic Fréchet kernel

We show in Banana–Doughnut I that a finite-frequency traveltime anomaly measured by cross-correlation of a windowed, observed pressure pulse $p^{obs}(t) = p(t) + \delta p(t)$ with a synthetic seismogram $p(t)$ is given, correct to first order in the perturbations δc and $\delta \rho$, by

$$\delta T = \frac{\int_{t_1}^{t_2} \dot{p}(t)\delta p(t)\, dt}{\int_{t_1}^{t_2} \ddot{p}(t) p(t)\, dt} = \frac{\mathscr{R}e \int_0^\infty i\omega\, p^*(\omega)\, \delta p(\omega)\, d\omega}{\int_0^\infty \omega^2 |p(\omega)|^2\, d\omega} , \quad (16)$$

where the asterisk denotes complex conjugation. A *negative* traveltime shift, $\delta T < 0$, corresponds to an *advance* in the arrival of the observed signal $p^{obs}(t)$ with respect to the synthetic signal $p(t)$, whereas a *positive* traveltime shift, $\delta T > 0$, corresponds to a *delay*. To simplify the integrals in (16), we replace the unperturbed Fourier transform $p(\omega)$ by the single phase of interest in the sum (9), but retain the summation over all possible singly scattered waves that may arrive during the cross-correlation time window $t_1 \le t \le t_2$ in the representation (14) of the perturbation $\delta p(\omega)$. The resulting traveltime shift of an acoustic wave can be written in a form analogous to (77)–(78) in Banana–Doughnut I:

$$\delta T = \iiint_{\oplus} \left[K_c \left(\frac{\delta c}{c}\right) + K_\rho \left(\frac{\delta \rho}{\rho}\right) \right] d^3\mathbf{x} , \quad (17)$$

where

$$K_{c,\rho} = -\frac{1}{2\pi c} \sum_{\text{rays}'} \sum_{\text{rays}''} \Omega_{c,\rho} \left(\frac{\mathscr{R}}{c_r \mathscr{R}' \mathscr{R}''} \right) \times \frac{\int_0^\infty \omega^3 |\dot{m}(\omega)|^2 \sin[\omega(T' + T'' - T) - (M' + M'' - M)\pi/2]\, d\omega}{\int_0^\infty \omega^2 |\dot{m}(\omega)|^2\, d\omega} . \quad (18)$$

The quantities K_c and K_ρ are the 3-D Fréchet kernels that relate a measured traveltime shift δT to the fractional perturbations $\delta c/c$, $\delta \rho/\rho$ in acoustic wave speed and density, respectively. The two factors

$$\Omega_c = 1 , \qquad \Omega_\rho = \frac{1}{2}(1 - \hat{\mathbf{k}}' \cdot \hat{\mathbf{k}}'') \quad (19)$$

are normalized *acoustic scattering coefficients* analogous to the 27 elastic scattering coefficients $\Omega_{\alpha,\beta,\rho}^{P,SV,SH \to P,SV,SH}$ in Banana–Doughnut I. Scattering off a point heterogeneity in wave speed δc is isotropic, whereas scattering off a density heterogeneity $\delta \rho$ is identically zero in the forward ($\hat{\mathbf{k}}'' = \hat{\mathbf{k}}'$) direction and maximal in the backward ($\hat{\mathbf{k}}'' = -\hat{\mathbf{k}}'$) direction, as illustrated in Fig. 2.

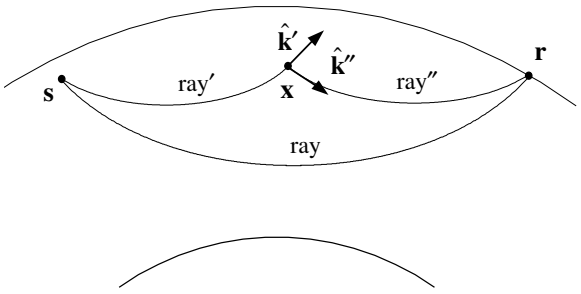

Figure 1. Cartoon cross-section of an acoustic mantle model showing the geometrical ray from a buried source $\mathbf{s}$ to a surface receiver $\mathbf{r}$. The Born approximation accounts for all singly scattered waves that propagate along a composite path ray$'$, ray$''$ from the source $\mathbf{s}$ to an arbitrary point heterogeneity $\mathbf{x}$, and then on to the receiver $\mathbf{r}$. The incoming and outgoing unit wave vectors at the scatterer $\mathbf{x}$ are $\hat{\mathbf{k}}'$ and $\hat{\mathbf{k}}''$, respectively.

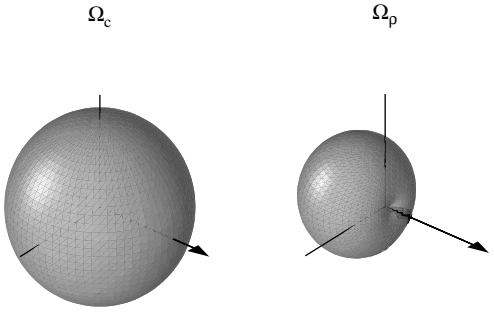

Figure 2. Perspective plots of the acoustic wave scattering coefficients Ω_c (left) and Ω_ρ (right). The orthonormal axes are centred upon the scatterer $\mathbf{x}$; arrows denote the direction of the incoming wave vector $\hat{\mathbf{k}}'$.

2.6 Boundaries

The attentive reader will have noted that we have made no mention of the boundary conditions associated with the differential equations (2)–(3). In fact, the above results are strictly valid only for a smooth infinite medium with no internal or external boundaries. More generally, the wave-speed and density Fréchet kernels (18) must be modified to account for the partition of incoming wave energy into outgoing transmitted and reflected energy at each boundary, by introducing the products Π, Π' and Π'' of $\pm(\text{energy})^{1/2}$ acoustic wave reflection coefficients along ray, ray′ and ray″, as in Banana–Doughnut I. In all of the spherical earth examples to be presented in this paper, we consider a smooth acoustic 'mantle' with no internal discontinuities, and an upper and lower boundary that are both *perfectly rigid*. The reflection coefficient of an acoustic pressure pulse at a rigid boundary is simply unity,

$$\Pi = \Pi' = \Pi'' = 1\,, \tag{20}$$

so that the kernels (18) are unaltered. If the two bounding surfaces are instead considered to be *free*, we must account for the reversal in the sign of $p(t)$ and $\delta p(t)$ upon every reflection; the kernels are then given by

$$K_{c,\rho} = -\frac{1}{2\pi c}\sum_{\text{rays}'}\sum_{\text{rays}''}(-1)^{N-N'-N''}\Omega_{c,\rho}\left(\frac{\mathscr{R}}{c_{\text{r}}\mathscr{R}'\mathscr{R}''}\right) \times \frac{\displaystyle\int_0^\infty \omega^3|\dot{m}(\omega)|^2\sin[\omega(T'+T''-T)-(M'+M''-M)\pi/2]\,d\omega}{\displaystyle\int_0^\infty \omega^2|\dot{m}(\omega)|^2\,d\omega}\,, \tag{21}$$

where N, N' and N'' are the number of free-surface reflections along the three paths ray, ray′ and ray″.

2.7 Paraxial kernel

In the paraxial approximation, we ignore all but forward ($\hat{\mathbf{k}}'' = \hat{\mathbf{k}}'$) scattering on nearby, like-type source-to-scatterer-to-receiver ray paths, and we approximate the various quantities in eq. (18) by

$$\Omega_c = 1\,, \quad \Omega_\rho = 0\,, \tag{22}$$

$$T' + T'' - T = \frac{1}{2}\,\mathbf{q}^{\text{T}}\cdot(\mathbf{M}'+\mathbf{M}'')\cdot\mathbf{q}\,, \tag{23}$$

$$\frac{\mathscr{R}}{c_{\text{r}}\mathscr{R}'\mathscr{R}''} = \sqrt{|\det(\mathbf{M}'+\mathbf{M}'')|}\,, \tag{24}$$

$$M' + M'' - M = \frac{1}{2}\,[\text{sig}\,(\mathbf{M}'+\mathbf{M}'') - 2]\,. \tag{25}$$

The matrices $\mathbf{M}' = \mathbf{M}_{\xi\text{s}}$ and $\mathbf{M}'' = \mathbf{M}_{\xi\text{r}}$ are the forward and backward 2×2 traveltime Hessians along the central ray $\mathbf{s}\le\boldsymbol{\xi}\le\mathbf{r}$, and $\mathbf{q} = \mathbf{x} - \boldsymbol{\xi}$ is the perpendicular distance of a scatterer $\mathbf{x}$ away from this ray, as illustrated in Fig. 3(a). The symbols det and sig denote the determinant and the signature, or the number of positive minus the number of negative eigenvalues, of the sum $\mathbf{M}'+\mathbf{M}''$, respectively. The paraxial traveltime expansion (23) is introduced, and the spreading factor and Maslov index relations (24)–(25) are verified, in Banana–Doughnut I.

A cross-correlation traveltime shift in this approximation is independent of the density, and dependent only upon the 3-D wave-speed perturbation:

$$\delta T = \iiint_{\oplus} K(\delta c/c)\,d^3\mathbf{x}\,. \tag{26}$$

The approximate Fréchet kernel K in eq. (26) is given by

$$K = -\frac{1}{2\pi c}\sqrt{|\det(\mathbf{M}'+\mathbf{M}'')|}\;\frac{\displaystyle\int_0^\infty \omega^3|\dot{m}(\omega)|^2\sin\Phi\,d\omega}{\displaystyle\int_0^\infty \omega^2|\dot{m}(\omega)|^2\,d\omega}\,, \tag{27}$$

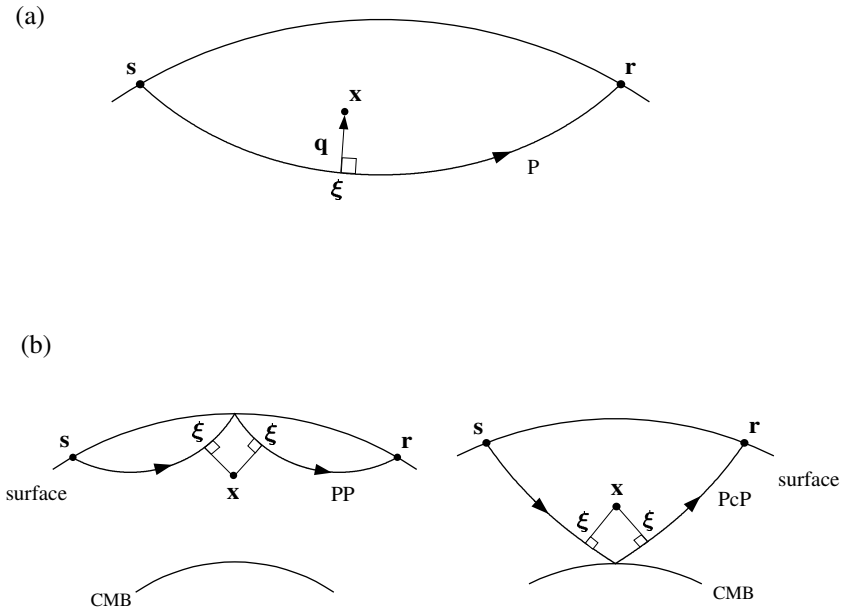

Figure 3. (a) In the paraxial approximation, every scatterer $\mathbf{x}$ is perpendicularly projected onto the nearest point ξ on the central geometrical ray from the source $\mathbf{s}$ to the receiver $\mathbf{r}$. The difference vector is $\mathbf{q} = \mathbf{x} - \xi$. (b) In many circumstances, including the two illustrated here, a scatterer can be projected onto more than one paraxial point $\boldsymbol{\xi}$. (Left) A scatterer in the vicinity of the surface reflection point of a *PP* wave. (Right) A scatterer in the vicinity of the core–mantle boundary (CMB) reflection point of a *PcP* wave.

where

$$\Phi = \frac{1}{2}\,\omega \mathbf{q}^{\mathrm{T}} \cdot (\mathbf{M}' + \mathbf{M}'') \cdot \mathbf{q} - [\mathrm{sig}\,(\mathbf{M}' + \mathbf{M}'') - 2]\pi/4\,. \tag{28}$$

Since $(-1)^{N'+N''-N}$ in the free-surface representation (21) is approximated by 1, the result (26)–(28) is applicable, regardless of the character of the upper and lower boundaries. We shall, in what follows, refer to K_c and K_ρ in (18) as the 'exact' ray-theoretical kernels, and we shall refer to K in (27) as the paraxial kernel. In the case of a compound ray such as *PP* or *PcP*, there may be more than one perpendicular projection point $\boldsymbol{\xi}$ for some scatterers $\mathbf{x}$, as illustrated in Fig. 3(b); the paraxial kernel K in such instances is a *sum* over all such central ray points $\boldsymbol{\xi}$.

2.8 Differential kernel

The first-order perturbation $\delta(\Delta T)$ in a differential traveltime,

$$\Delta T = T_{\mathrm{B}} - T_{\mathrm{A}}\,, \tag{29}$$

measured by cross-correlation of two observed body wave arrivals $p_{\mathrm{A}}^{\mathrm{obs}}(t) = p_{\mathrm{A}}(t) + \delta p_{\mathrm{A}}(t)$ and $p_{\mathrm{B}}^{\mathrm{obs}}(t) = p_{\mathrm{B}}(t) + \delta p_{\mathrm{B}}(t)$ is likewise a linear functional of the 3-D wave-speed and density heterogeneity:

$$\delta(\Delta T) = \iiint_{\oplus} \left[K_c \left(\frac{\delta c}{c} \right) + K_\rho \left(\frac{\delta \rho}{\rho} \right) \right] d^3\mathbf{x}\,. \tag{30}$$

As in Banana–Doughnut I, we restrict attention to the only case of practical interest, in which the Maslov indices and, therefore, the pulse shapes of the two phases are identical:

$$M_{\mathrm{A}} = M_{\mathrm{B}} \Rightarrow \dot{m}_{\mathrm{H}}^{(M_{\mathrm{A}})}(t) = \dot{m}_{\mathrm{H}}^{(M_{\mathrm{B}})}(t)\,. \tag{31}$$

Each of the differential Fréchet kernels $K_{c,\rho}$ in (23) is then simply the *difference of the kernels for the individual phases*, i.e.

$$K_{c,\rho}^{\mathrm{B-A}} = K_{c,\rho}^{\mathrm{B}} - K_{c,\rho}^{\mathrm{A}} \quad \text{if} \quad M_{\mathrm{A}} = M_{\mathrm{B}}\,. \tag{32}$$

A similar remark obviously applies to the paraxial kernels:

$$\delta(\Delta T) = \iiint_{\oplus} K(\delta c/c)\, d^3\mathbf{x}\,, \tag{33}$$

where

$$K^{\mathrm{B-A}} = K^{\mathrm{B}} - K^{\mathrm{A}} \quad \text{if} \quad M_{\mathrm{A}} = M_{\mathrm{B}}\,. \tag{34}$$

The physically plausible results (32) and (34) reduce the problem of computing differential Fréchet kernels to pointwise subtraction.

2.9 Reduction to ray theory

In the limit of high frequency, $\omega \to \infty$, it is possible to evaluate the 2-D integral over the transverse coordinates $\mathbf{q} = (q_1, q_2)$ in the paraxial representation (26) by the *method of stationary phase*. The resulting traveltime shift is exactly that predicted by geometrical ray theory:

$$\delta T_{\mathrm{ray}} = -\int_{\mathbf{s}}^{\mathbf{r}} c^{-2}\delta c\, dl\,. \tag{35}$$

As is well known, Fermat's principle enables the integration in (35) to be carried out along the *unperturbed* ray.

3 NUMERICAL VALIDATION

We begin by considering an extremely simple example—a single, smooth, spherical, cosine-bell 'inclusion' in an otherwise infinite homogeneous medium. The anomaly is situated at the centre of a $4000 \times 4000 \times 4000$ km^3 cube, as depicted in Fig. 4; an explosive point source is detonated at a point $\mathbf{s}$ near one of the corners of the cube, and the wavefield and traveltimes are sampled at a fan-shaped array of equidistant receivers $\mathbf{r}$ in the vicinity of the diagonally opposite corner. We denote the position of an individual receiver $\mathbf{r}$ by its azimuth 0°, 5°, ..., 85°, 90°; the middle or 45° receiver lies along the straight-ray path through the spherically symmetric anomaly. The linear distance from the source to each of the 19 receivers is $\|\mathbf{r} - \mathbf{s}\| = 4000$ km; the centre of the anomaly is halfway between the source and the 45° receiver.

We investigate the effect of both 'slow' and 'fast' anomalies, having $\delta\rho = 0$ and a wave-speed perturbation of the form

$$\delta c = \begin{cases} \delta c_0[1 + \cos(2\pi r/a)] & \text{if } r \le a/2 \\ 0 & \text{if } r \ge a/2 \end{cases}, \tag{36}$$

where r is the radial distance from the centre. We also consider a pure density anomaly, having $\delta c = 0$ and the same cosine-bell shape:

$$\delta\rho = \begin{cases} \delta\rho_0[1 + \cos(2\pi r/a)] & \text{if } r \le a/2 \\ 0 & \text{if } r \ge a/2 \end{cases}. \tag{37}$$

The background wave speed and density are $c = 8$ km and $\rho = 3300$ kg m^{-3}, respectively.

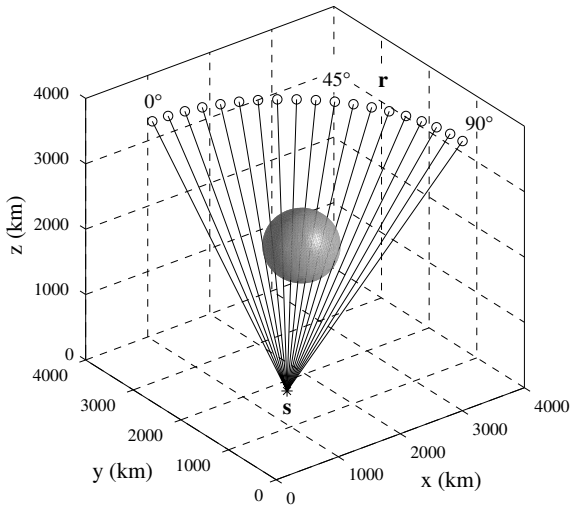

Figure 4. Model configuration and source–receiver geometry used in numerical simulation of 3-D scalar-wave propagation. The shaded isosurface represents a smooth, spherically symmetric wave-speed or density anomaly embedded in an otherwise homogeneous background medium. Solid lines are the unperturbed straight rays between the source $\mathbf{s}$, denoted by an asterisk, and an array of equidistant receivers $\mathbf{r}$, denoted by open circles. The azimuth of the receivers varies from 0° to 90°, so that some of the rays sample the anomaly, whereas others do not.

3.1 Source-time function

The time variation of the differential source volume in eq. (3) is assumed to be a Gaussian, of the form

$$m(t) = \exp\left[-4\pi^2\left(\frac{t}{\tau}-\frac{1}{2}\right)^2\right]. \tag{38}$$

The resulting pressure response in the background homogeneous medium is an acausal full-cycle pulse,

$$\dot{m}(t) = -8\pi^2\tau^{-2}\left(t-\frac{1}{2}\,\tau\right)\exp\left[-4\pi^2\left(\frac{t}{\tau}-\frac{1}{2}\right)^2\right], \tag{39}$$

that is first manifestly different from zero at $t=0$. The associated power spectrum

$$|\dot{m}(\omega)|^2 = (\omega^2\tau^2/4\pi)\exp(-\omega^2\tau^2/8\pi^2) \tag{40}$$

has its centroid and its maximum at

$$\omega_{\rm cen} = \sqrt{2}(2\pi/\tau), \qquad \omega_{\rm max} = 2\sqrt{2/\pi}\,(2\pi/\tau), \tag{41}$$

respectively. We shall, in the discussion that follows, refer to τ as the characteristic period of the pulse (39), and to $\lambda = c\tau$ as the associated characteristic wavelength. It is, however, clear from (41) that the dominant or 'visual' period and wavelength are about 1.5 times shorter than this:

$$\tau_{\rm vis}/\tau \approx \lambda_{\rm vis}/\lambda \approx 1/\sqrt{2} \approx \frac{1}{2}\sqrt{\pi/2}. \tag{42}$$

Since $\dot{m}(t)$ is a full-cycle (up, then twice as far down, then back up) rather than a half-cycle (up, then back down) pulse, the pressure response $p(t)$ simulates a ground-velocity rather than a ground-displacement body wave seismogram.

3.2 Pseudospectral synthetic seismograms

A parallelized pseudospectral method was used to solve eqs (2)–(3) numerically. The anisotropic, elastic code of Hung & Forsyth (1998) was adapted for this purpose. In this method, the wavefield variables p and $\mathbf{u}$ are represented as discrete 3-D Fourier expansions, enabling the spatial derivatives ∇p and $\boldsymbol{\nabla}\cdot\mathbf{u}$ to be computed by multiplication in the wavenumber domain. Grid dispersion is minimal in comparison to finite difference methods, which use only a few neighbouring nodes to approximate the spatial derivatives. A conventional fourth-order Runge–Kutta scheme was used to advance p and $\mathbf{u}$ in time. An absorbing boundary condition described by Cerjan *et al.* (1985) was utilized on each of the eight faces of the cube, to suppress artificial reflections. The pressure response at receivers $\mathbf{r}$ between gridpoints was computed by means of a 3-D bilinear interpolation from the eight adjacent nodal values. Computer memory and time considerations dictated the use of a relatively long-period source pulse, $\tau = 50$ s ($\tau_{\rm vis} = 30$–35 s). The numerical implementation was fully tested by comparison with the exact analytical solution (7) in the background homogeneous medium.

Table 1 lists the parameters utilized for a suite of 'single-spherical-scatterer' numerical validation experiments. The width a and average fractional amplitude $\delta c_0/c$ of each of the wave-speed anomalies (36) have been chosen to ensure that the maximum geometrical advance or delay (35) is always the same, $\delta T_{\rm ray} = \pm 3$ s. The corresponding ray-theoretical traveltime shift for a density anomaly (37) is, of course, zero. The most critical parameter governing the validity of ray theory is the ratio a/λ of the characteristic scale length of the 3-D heterogeneity to the characteristic wavelength of the wave. Roughly speaking, we expect ray theory to pertain whenever this ratio significantly exceeds unity, $a/\lambda \gg 1$.

Fig. 5 shows a suite of synthetic waveforms for a relatively concentrated, relatively strong wave-speed anomaly (Case 1: $a/\lambda = 1.5$, $\delta c_0/c = \pm 4$ per cent) and a broader, more subdued one (Case 3: $a/\lambda = 10$, $\delta c_0/c = \pm 1.5$ per cent); the corresponding seismograms in the background homogeneous medium are superimposed for comparison. The waveform perturbations produced by a strong, concentrated anomaly are extremely subtle. Clearly, no matter how the traveltime shifts at the receivers in the vicinity of 45° are measured, they will be much less than those predicted by geometrical ray theory, $\delta T_{\rm ray} = \pm 3$ s. On the other hand, the arrivals near 45° in the case of a broad, subdued anomaly are either advanced or delayed by about this expected amount. Other ray-theoretical effects are also visible in this latter case; in particular, the maximum amplitude of the 45° pulse is increased in the case of a slow anomaly ($\delta c < 0$) and decreased in the case of a fast one ($\delta c > 0$), as a result of geometrical focusing and defocusing, respectively. Synthetic seismograms were also computed for a suite of models having a density heterogeneity $\delta\rho$ rather than a wave-speed heterogeneity δc (Cases 4–6). The resulting waveform perturbations were all indiscernible to the naked eye at the level of resolution shown here.

3.3 Fréchet kernel geometry

In this simple case of a homogeneous background medium, there is a single straight ray′ from the source $\mathbf{s}$ and a single

Table 1. Summary of parameters used in the numerical validation experiments: τ is the characteristic period of the unperturbed pressure pulse $\dot{m}(t)$ and $\lambda = c\tau$ is the associated characteristic wavelength; a is the characteristic width of the bell-shaped anomaly and $\delta c_0/c$ and $\delta\rho_0/\rho$ are the average fractional perturbations; $L = 4000$ km is the invariant distance between the source $\mathbf{s}$ and the receiver $\mathbf{r}$.

Case	τ (s)	λ (km)	a (km)	L (km)	$\delta c_0/c$ (%)	$\delta\rho_0/\rho$ (%)	a/λ	L/λ	L/a	$\delta T_{\rm ray}$ (s)
1	50	400	600	4000	±4	–	1.5	10	6.67	±3
2	50	400	1000	4000	±2.4	–	2.5	10	4	±3
3	20	160	1600	4000	±1.5	–	10	25	2.5	±3
4	50	400	600	4000	–	±4	1.5	10	6.67	0
5	50	400	1000	4000	–	±2.4	2.5	10	4	0
6	20	160	1600	4000	–	±1.5	10	25	2.5	0

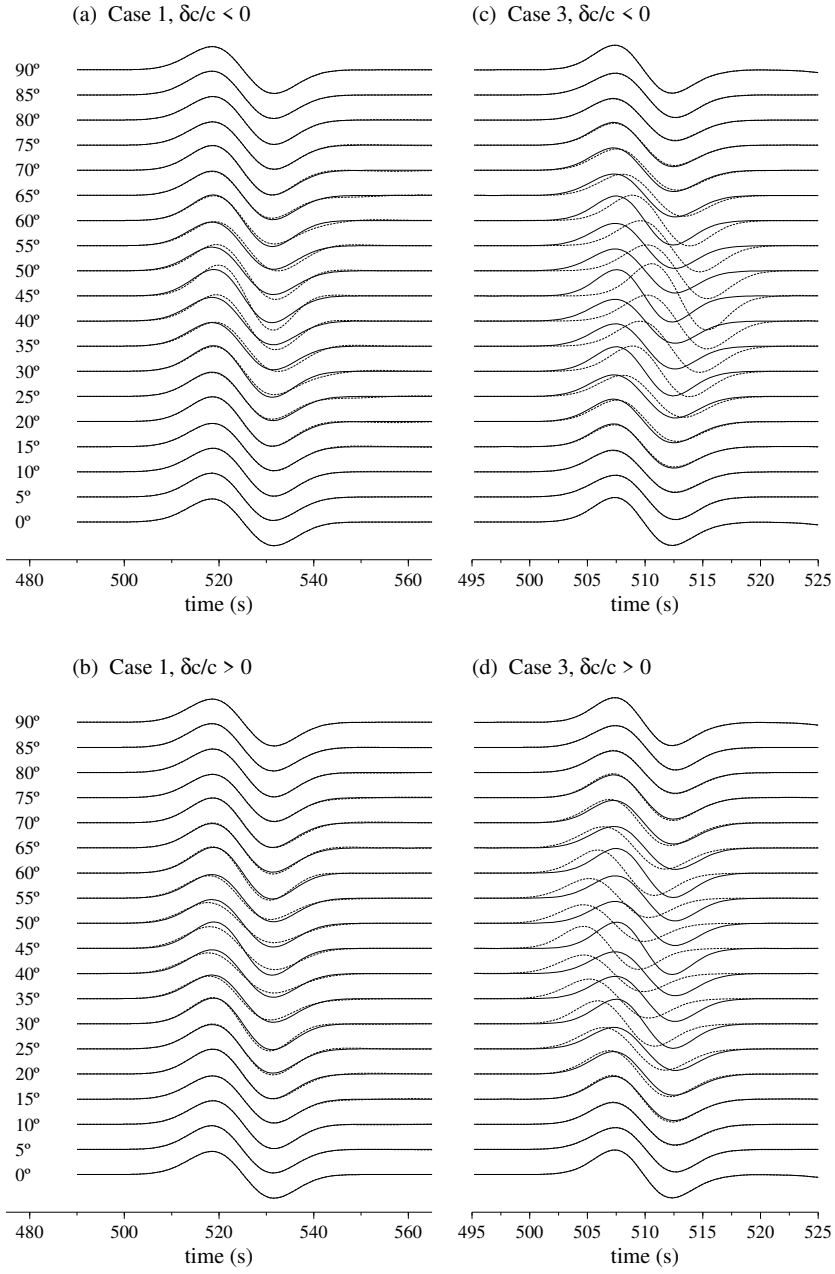

Figure 5. Synthetic pressure-response seismograms $p(t)$, computed using the pseudospectral method. All of the receivers are situated at the same distance from the source, $\|\mathbf{r}-\mathbf{s}\|=4000$ km; the azimuths 0°, 5°, ..., 85°, 90° are indicated on the left. Identical solid lines show the unperturbed seismograms in the homogeneous background medium; dashed lines show the effect of a spherically symmetric, slow (top) or fast (bottom) perturbation in the acoustic wave speed. (a) Case 1: $a/\lambda=1.5$, $\delta c_0/c=-4$ per cent. (b) Case 1: $a/\lambda=1.5$, $\delta c_0/c=+4$ per cent. (c) Case 3: $a/\lambda=10$, $\delta c_0/c=-1.5$ per cent. (d) Case 3: $a/\lambda=10$, $\delta c_0/c=+1.5$ per cent. It is evident that cross-correlation is the only viable means of measuring the traveltime shift δT of such a long-period waveform. The effect of wave-speed heterogeneity δc differs for different segments of the pulse; traditional seismological methods that focus upon a single characteristic such as an analyst-picked onset or the maximum would be quite arbitrary, as well as prone to errors due to noise.

straight ray″ from the receiver $\mathbf{r}$ to the scatterer $\mathbf{x}$. The traveltimes, Maslov indices and geometrical spreading factors in eq. (18) are given by

$$T=\frac{\|\mathbf{r}-\mathbf{s}\|}{c}\,,\qquad T'=\frac{\|\mathbf{x}-\mathbf{s}\|}{c}\,,\qquad T''=\frac{\|\mathbf{x}-\mathbf{r}\|}{c}\,, \tag{43}$$

$$M=M'=M''=0\,, \tag{44}$$

$$\mathscr{R}=\|\mathbf{r}-\mathbf{s}\|\,,\qquad \mathscr{R}'=\|\mathbf{x}-\mathbf{s}\|\,,\qquad \mathscr{R}''=\|\mathbf{x}-\mathbf{r}\|\,. \tag{45}$$

The resulting 'exact' Fréchet traveltime kernels K_c and K_ρ for a $\tau=50$ s acoustic wave are depicted in Fig. 6. The receiver $\mathbf{r}$ is at azimuth 45°; the superimposed black circles show the $\delta c/c=0$, ±2, ±4, ±6 per cent contours of an $a=1.5\lambda$, $\delta c_0/c=\pm4$ per cent (i.e. $|\delta c_{\max}|/c=8$ per cent) anomaly for comparison. The banana–doughnut character of both kernels is evident—although perhaps 'cigar–doughnut' would be a more apt metaphor in this straight-ray instance! In a ray-plane cross-section, both K_c and K_ρ exhibit an elliptical shape,

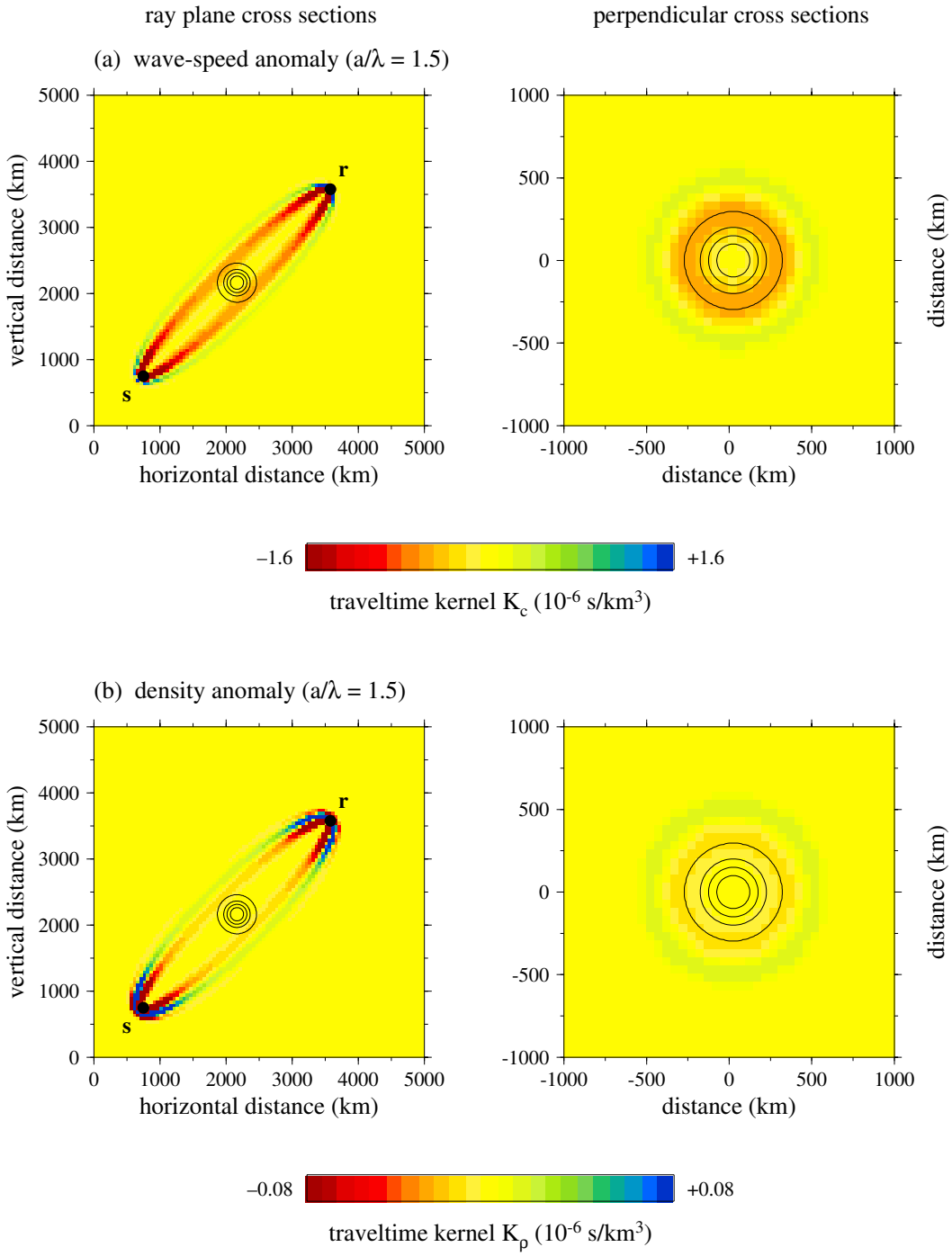

Figure 6. Cross-sections of the 3-D traveltime Fréchet kernels in a homogeneous background medium for a receiver at a distance $\|\mathbf{r}-\mathbf{s}\|=4000$ km and an azimuth of 45°. The characteristic period of the Gaussian-derivative wavelet $\dot{m}(t)$ is $\tau=50$ s. (a) Sensitivity K_c to a fractional change $\delta c/c$ in wave speed. (b) Sensitivity K_ρ to a fractional change $\delta\rho/\rho$ in density. Left panels show a ray-plane cross-section passing through the source **s** and receiver **r**; right panels show a path-perpendicular cross-section, through the source–receiver midpoint. Circular contours show the location and size of a Case 1 or Case 4 anomaly. The outer circle, of radius $a=1.5\,\lambda$, is where the smooth, cosine-bell perturbation (36) or (37) vanishes.

whereas in a cross-section perpendicular to the ray path, they are circularly symmetric, with a yellow hollow interior flanked by red ($K_{c,\rho}<0$) side lobes. This yellow-to-red region can be regarded as the (broad-band) first Fresnel zone, within which

$$0\le\bar{\omega}(T'+T''-T)\le\pi\,, \tag{46}$$

where $\bar{\omega}\approx\omega_{\rm cen}\approx\omega_{\rm max}$ is the dominant frequency of the pulse (39). The fringing green ($K_{c,\rho}>0$) sidelobes lie within the second Fresnel zone, where $\pi\le\bar{\omega}(T'+T''-T)\le2\pi$. The absolute magnitude of the kernels is significantly reduced in this as well as the surrounding higher-order Fresnel zones as a result of destructive interference among adjacent frequencies ω and $\omega+d\omega$ in the integral (18).

Finally, we note that the overall magnitude of the density kernel is everywhere much less than that of the wave-speed kernel: $|K_\rho|\ll|K_c|$. The reason for this is evident: destructive

interference limits the contribution of all scattering interactions that are not nearly forward ($\hat{\mathbf{k}}'' \approx \hat{\mathbf{k}}'$), and forward scattering off a density heterogeneity is extremely inefficient:

$$\Omega_\rho = \frac{1}{2}\,(1 - \hat{\mathbf{k}}' \cdot \hat{\mathbf{k}}'') \approx 0\,. \tag{47}$$

The upshot of this is hardly a surprise—a traveltime shift δT is much less sensitive to density heterogeneity $\delta\rho$ than to wave-speed heterogeneity δc. Homogeneous-medium Fréchet kernels with properties similar to those presented here have been discussed previously by Woodward (1992), Yomogida (1992) and Vasco & Majer (1993).

3.4 Traveltime comparison

Synthetic traveltime shifts δT were measured for all of the cases considered by cross-correlation of the perturbed and unperturbed pseudospectral seismograms. The time window $t_1 \le t \le t_2$ was chosen conservatively, to ensure that we always included essentially the entire two-sided pulse $\dot{m}(t)$. The values of δT were determined by least-squares fitting of a parabola to the digital cross-correlagram in the vicinity of its maximum. Fig. 7 compares the measured cross-correlation traveltime shifts with the theoretical predictions of both Born–Fréchet kernel theory (17)–(18) and geometrical ray theory (35). As expected on the basis of the above discussion, a slow

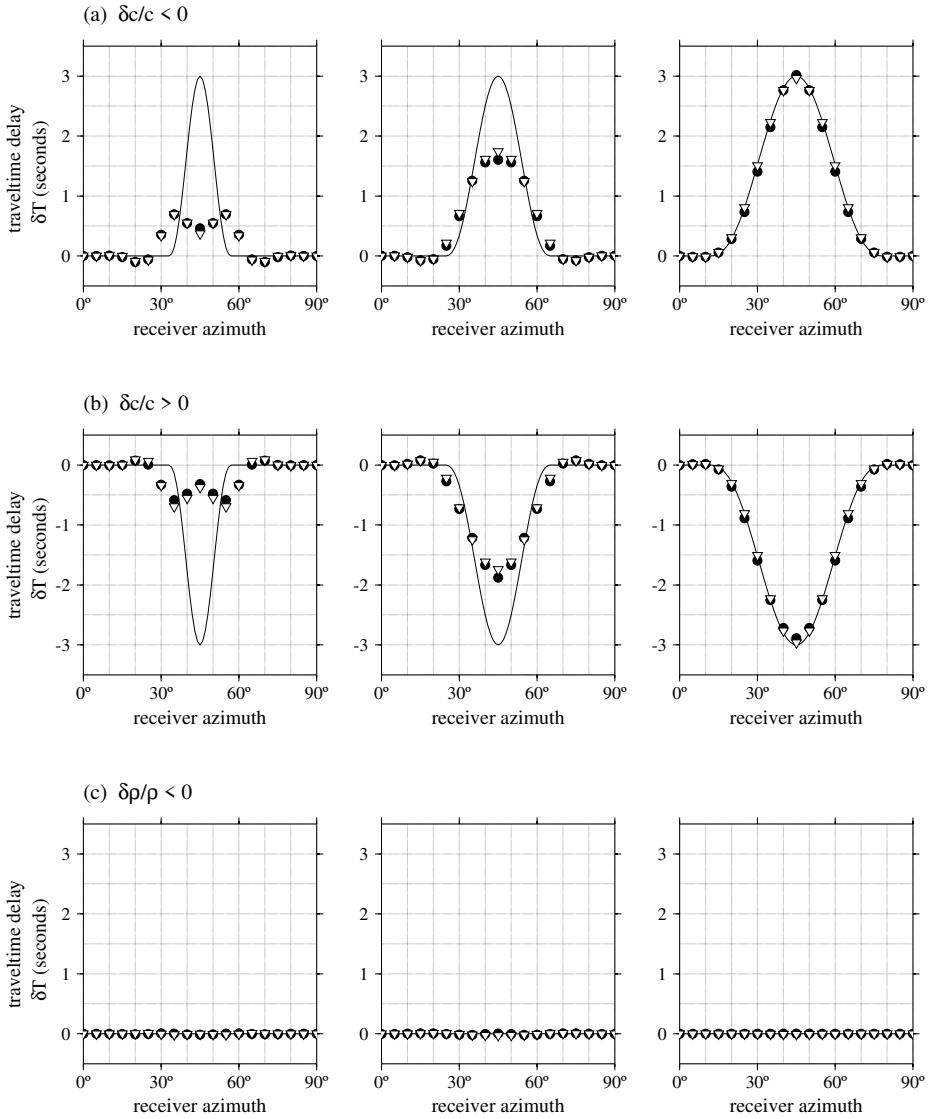

Figure 7. Traveltime anomaly δT versus receiver azimuth. Solid circles are the traveltimes measured by cross-correlation of the pseudospectral synthetic seismograms; unfilled inverted triangles are the theoretical traveltimes computed using the Born Fréchet kernels K_c and K_ρ; smooth curve shows the Fermat straight-ray approximation. (a) Slow wave-speed anomalies: Cases 1 to 3 (left to right). (b) Fast wave-speed anomalies: Cases 1 to 3 (left to right). (c) Density anomalies: Cases 4 to 6 (left to right). Wave-front healing and diffraction reduce the magnitudes of the traveltime shifts produced by both a concentrated (Case 1) and a quasi-concentrated (Case 2) wave-speed anomaly. The traveltime shifts produced by a smoother (Case 3) anomaly are, in contrast, in good agreement with geometrical ray theory. A modest density anomaly produces an imperceptible traveltime shift, no matter how it is measured.

or fast concentrated wave-speed anomaly (Case 1: $a/\lambda = 1.5$, $\delta c_0/c = \pm 4$ per cent) gives rise to a relatively small traveltime shift, whereas a broader anomaly (Case 3: $a/\lambda = 10$, $\delta c_0/c = \pm 1.5$ per cent) gives rise to a more substantial shift that is in good agreement with ray theory ($\delta T \approx \delta T_{\rm ray}$). An 'intermediate' wave-speed anomaly (Case 2: $a/\lambda = 2.5$, $\delta c_0/c = \pm 2.4$ per cent) gives rise to an 'intermediate' traveltime shift, whose maximum at the 45° receiver is slightly reduced from the ray-theoretical maximum, $\delta T_{\rm ray} = \pm 3$ s, as a result of diffraction and wave-front healing. All three density anomalies (Cases 4–6) give rise to a negligible traveltime shift, $\delta T \approx 0$, as expected.

In every case, the measured traveltime shift is in excellent agreement with the shift computed by integration with the Fréchet kernel K_c or K_ρ. This is the most important finding of the present numerical study, since it validates our Born–Fréchet kernel theory, both in situations where ray theory is applicable, as well as in situations where it is not. In the example considered here, the lateral refraction of geometrical rays is relatively slight, so there are no caustics or triplications in the vicinity of any of the receivers **r**. In addition, the maximum traveltime anomalies are substantially less than the characteristic period of the waves ($|\delta T_{\rm ray}| \approx \tau_{\rm vis}/10$), so there is no possibility of confusion due to a cycle skip. This is the proper province of the Born approximation.

It is noteworthy that the maximum absolute traveltime shift produced by a concentrated wave-speed anomaly is *not* observed at the 45° receiver; rather, there is a local minimum in $|\delta T|$ at 45°, with maxima at azimuths 35° and 55°. This is an extremely unintuitive result on the basis of naive ray-theoretical considerations; however, it is a natural consequence of the banana–doughnut character of the wave-speed kernel K_c. A sufficiently small heterogeneity $\delta c_0/c$ can fit inside the yellow doughnut hole of the 45° kernel, and thus give rise to a negligible traveltime shift δT. At 35° and 55° the anomaly $\delta c_0/c$ is situated within the red doughnut itself, where $|K_c|$ is maximal. In this way, a concentrated off-path anomaly can give rise to a larger traveltime shift than one directly on the ray path. Inspection of the synthetic seismograms in Fig. 5 suggests that the minimum at 45° would *not* be present if δT were measured by hand-picking the 'onset' or first 'break' of the arrivals. In a cross-correlation measurement, however, the entire pulse contributes to the traveltime shift. The principal difference between the perturbed and unperturbed seismograms at 45° is the steeper downswing following the initial upswing in the case of a slow anomaly, $\delta c < 0$, and the more gradual downswing in the case of a fast anomaly, $\delta c > 0$. In essence, diffraction by a slow or fast anomaly shifts a fraction of the total energy to earlier or later times in the downswing, leading to a reduced—in fact locally minimal—absolute traveltime shift $|\delta T|$.

We note finally that at the receivers in the vicinity of 20° and 70°, the traveltime shifts produced by a concentrated anomaly are actually of the 'opposite' sign—fast, $\delta T < 0$, for a slow anomaly, $\delta c < 0$, and slow, $\delta T > 0$, for a fast anomaly, $\delta c > 0$. This result is particularly perplexing on the basis of naive considerations, since in the latter case it appears to violate the principle of causality. The Fréchet kernel provides a ready explanation: the centre of the anomaly is in this case situated in the second (green) Fresnel zone, where K_c is positive. Blow-ups of the synthetic seismograms in Fig. 5 reveal that the first 'breaks' do respect causality, as of course they must. The principal discrepancy between the 20° and 70° perturbed and unperturbed seismograms is in the tails.

3.5 Wielandt effect

A previous numerical investigation of scattering and diffraction by a single spherical inclusion has been conducted by Wielandt (1987). He considered a sphere with a *constant* wave-speed perturbation δc; this problem of a hard acoustic scatterer has a well-known analytical solution (Sommerfeld 1949). An automated picking method was used to measure synthetic traveltimes rather than cross-correlation; the 'onset' of every pulse was defined to be the point at which its amplitude first exceeded 15 per cent of its peak value. Using this technique, Wielandt observed a large and consistent difference in the character of the measured traveltimes, depending upon the *sign* of the anomaly. Positive traveltime shifts produced by a slow ($\delta c < 0$) sphere were significantly reduced by wave-front healing, whereas negative shifts produced by a fast ($\delta c > 0$) sphere were in much better agreement with ray theory. The physical explanation for this slow–fast asymmetry is straightforward: waves diffracted around the boundary of a slow sphere are able to arrive significantly before the straight-ray geometrical arrival, whereas no such faster diffracted path exists in the case of a fast anomaly. The upshot of such a diffraction-induced asymmetry in teleseismic traveltimes would be a bias towards faster wave speeds in a 3-D inversion. This *Wielandt effect* has subsequently been studied by a number of investigators, in both 2-D and 3-D pseudo-random models, using a variety of finite difference, ray-theoretical, eikonal and Fourier wave-front-migration methods (e.g. Müller *et al.* 1992; Roth *et al.* 1993; Nolet & Moser 1993; Witte *et al.* 1996; Gudmundsson 1996). There is a very slight slow–fast asymmetry in the cross-correlation traveltimes (solid circles) in Fig. 7, but the effect is of variable sign, depending upon the circumstances, and much smaller than that observed for picked times by Wielandt. This is in accordance with Born–Fréchet kernel theory, which predicts that there should be no slow–fast asymmetry whatsoever for slight traveltime shifts measured by cross-correlation. A change in the sign of the wave-speed anomaly, $\delta c \rightarrow -\delta c$, in eq. (17) or (26) simply changes the sign of the traveltime anomaly, $\delta T \rightarrow -\delta T$. Nolet & Dahlen (1999) find an analogous slow–fast asymmetry, which is more significant for larger values of the fractional traveltime anomaly $|\delta T|/\tau_{\rm vis}$, in their analysis of the healing of a wave front with an initial delay or advance in a homogeneous medium. The slow–fast asymmetry and the associated error in the Born–Fréchet linearization (17)–(18) are also likely to be larger in the present case for larger-amplitude anomalies $\pm \delta c/c$.

4 RAY-THEORETICAL KERNEL

In this section, we present a number of examples of 3-D Fréchet kernels K_c for a slightly more realistic seismological situation—a smooth, spherically symmetric mantle model with a radial wave-speed profile given by

$$c(r) = (r/a)[c_0 + c' a \ln(a/r)] \quad \text{in } b \le r \le a\,, \tag{48}$$

where

$$a = 6371 \text{ km}\,, \quad b = 3471 \text{ km} \tag{49}$$

and

$$c_0 = 4.5 \text{ km s}^{-1}, \quad c' = 0.0025 \text{ s}^{-1}. \tag{50}$$

The parameters (49)–(50) have been chosen to simulate the propagation of shear rather than compressional waves; the wave speed increases monotonically from its surface value $c_0 = 4.5$ km s^{-1} at $a = 6371$ km to a maximum $c_{\max} = 7.7$ km s^{-1} at the core–mantle boundary $b = 3471$ km, as illustrated in Fig. 8. Because of the rigid upper boundary conditions (20), the results presented here are best regarded as kernels for horizontally polarized SH, SS_{SH}, ScS_{SH}, ... waves; in the spirit of acoustic correctness, however, we shall refer to the various waves and associated kernels as P, PP, PcP, ... The particular analytical form of the wave-speed profile (48) was chosen to expedite the two-point ray tracing from the source **s** and receiver **r** to an arbitrary scatterer **x**. The details of the quasi-analytical procedures used to trace rays are described in Appendix A.

We restrict attention for the time being to a source **s** situated upon the earth's surface. Fig. 9 summarizes the various scattering paths that must then be taken into account in computing a ray-theoretical Fréchet kernel K_c. Each ray′ or ray″ in the double sum (18) is characterized by the number of reflections it experiences off either the upper or lower surface between the source **s** or the receiver **r** and the scatterer **x**. A reflection off the core–mantle boundary may either arrive directly at the scatterer **x** from below, or proceed on to reflect again off the top surface to arrive at **x** from above. A reflection off the upper surface that does not encounter the core–mantle boundary is a special case, since depending upon its location, a scatterer **x** may have either no or two such incoming rays′ or rays″. A scatterer situated above the source-to-receiver caustic has two incoming surface-reflected rays′, one that has passed through the caustic and arrives from below, and another that has not yet passed through the caustic and arrives from above. Similar remarks apply to the backward rays″ and the receiver-to-source caustic, so that these two caustics partition 'scatterer space' into four distinct regions, as illustrated in Fig. 10. In all the examples considered here, we have summed all rays′ and rays″ having two or fewer reflections off the upper surface and the core–mantle boundary. This is purposeful overkill, since our intent is to compute bona fide 'exact' (ray′ + ray″) Fréchet kernels K_c. In practice, the only significant contributions to K_c come from like-type scattering paths with traveltimes $T' + T'' \approx T$.

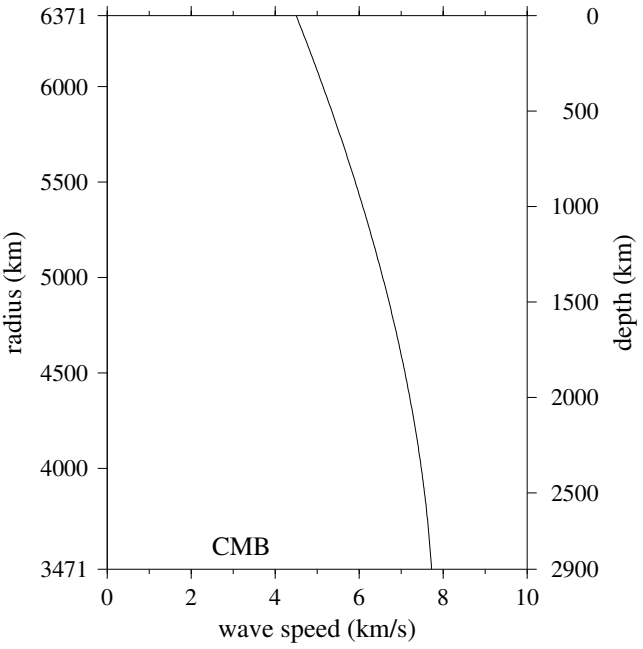

Figure 8. Variation of acoustic wave speed $c(r)$ versus depth $h = a - r$ in the model (48)–(50). The core–mantle boundary (CMB) is situated at a depth $h = 2900$ km.

To display the kernels, we use the spherical polar coordinate system depicted in Fig. 11. The source **s** and receiver **r** are both situated on the equator, at colatitude $\theta = 90°$, and longitudes $\phi = 0$ and $\phi = \Delta$, respectively. The quantity Δ is the angular epicentral distance; geometrical rays between **s** and **r** are confined to the equatorial source–receiver plane. To visualize the inherently 3-D kernels on the printed page, we resort to 2-D cross-sections, at fixed colatitude θ, longitude ϕ or depth $h = a - r$.

4.1 *P* wave

In Fig. 12 we display a number of cross-sectional views of the wave-speed kernel K_c for a direct P wave at an epicentral distance $\Delta = 60°$. Two different characteristic periods are considered, $\tau = 10$ s and $\tau = 20$ s. Fig. 12(a) depicts the two ray-plane cross-sections at constant colatitude $\theta = 90°$; Fig. 12(b) depicts several sections that cut quasi-perpendicularly across the ray path, at constant longitude, $\phi = 30°$ and $\phi = 45°$; Fig. 12(c) displays the kernel for a $\tau = 20$ s wave on three vertical slices parallel to the ray plane, at colatitudes $90° \pm 1°$, $90° \pm 2°$, $90° \pm 3°$. The now familiar banana–doughnut character of the kernel is again apparent. The sensitivity is yellow, or identically zero, everywhere along the geometrical ray path; the maximum sensitivity is in the red outer part of the first Fresnel zone, where $K_c < 0$. This in turn is surrounded by a faint green second Fresnel zone, where $K_c > 0$. The black curves in Fig. 12(a) show the radial dependence of the sensitivity along a line passing through the turning point at $\phi = 30°$. These 1-D representations illustrate the zero sensitivity along the ray, and the surrounding zones where $K_c < 0$ and $K_c > 0$, particularly clearly. For a fixed source–receiver geometry, the cross-path extent or 'fatness' of the kernel K_c varies as the square root $\sqrt{\tau}$ of the characteristic period of the wave; the $\tau = 20$ s kernel is for this reason $\sqrt{2}$ times as 'fat' as the $\tau = 10$ s kernel. The kernel for an even shorter-period wave, $\tau \ll 20$ s, would be an extremely slender hollow banana. Finally, we note that the acoustic wave kernels presented here agree extremely well with the SH-wave kernels computed by Marquering *et al.* (1999) using surface wave rather than body wave summation. We have not attempted a more quantitative comparison, inasmuch as the wave-speed profiles and the source time functions are slightly different in the two studies.

4.2 *PP* wave

The traveltimes of PP and SS surface reflections are widely used in seismic tomography because of their unique ability to probe the structure of the upper mantle beneath the bounce point, in regions that may not be well sampled by subsource and subreceiver rays (e.g. Kuo *et al.* 1987; Sheehan & Solomon

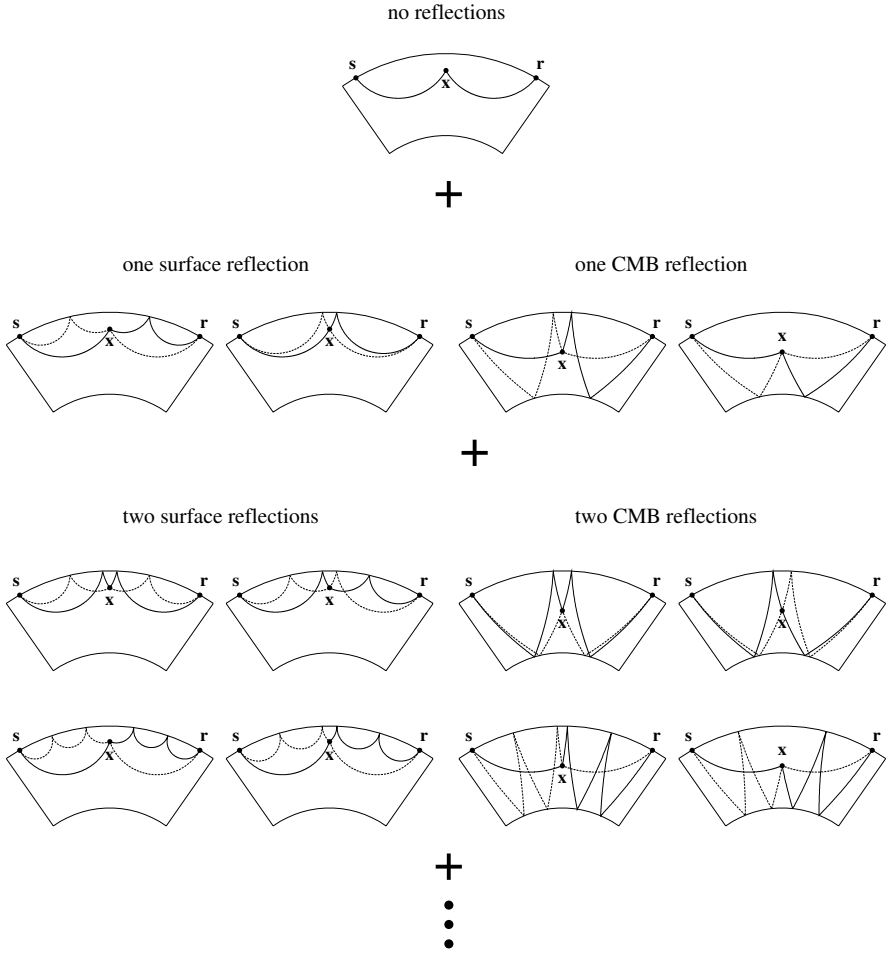

Figure 9. Pictorial glossary of the possible composite ray paths from a surface source **s** to a surface receiver **r**. Each path has a single non-Snell interaction at a (usually buried but possibly surficial) scatterer **x**. Solid and dotted lines distinguish cases in which there are multiple single-scattering paths from **s** to **r**, with a given number of reflections off the free surface or the core–mantle boundary (CMB). In principle, all of these ray′, ray″ combinations must be accounted for in evaluating the double sum (18).

1991; Woodward & Masters 1991; Neele & Snieder 1992; Paulssen & Stutzman 1996; Neele *et al.* 1997; Neele & de Regt 1999; Shearer *et al.* 1999). In Fig. 13, we display a number of cross-sections through the 3-D Fréchet kernel K_c for a $\tau = 20$ s *PP* wave at an epicentral distance $\Delta = 60^\circ$. Visual comparison with the surface wave-sum *SS* kernel of Marquering *et al.* (1999) shows that its previously rather poorly understood geometrical complexity is faithfully reproduced. The present formulation provides a simple physical interpretation of the principal features of this complicated 3-D geometry, in terms of the traveltimes T, T', T'' and Maslov indices M, M', M'' of the contributing body waves.

The *PP* wave from **s** to **r** passes through the source-to-receiver caustic, where it experiences a non-geometrical $\pi/2$ phase shift, at $\phi = 2\Delta/3 = 40^\circ$. The backward wave from **r** to **s** likewise passes through the receiver-to-source caustic at $\phi = \Delta/3 = 20^\circ$. The presence of these two caustics is responsible for the fundamental change in the character of the kernel *along* the geometrical *PP* ray. This change is most obvious in the ray-plane cross-section exhibited in Fig. 13(a): the traveltime sensitivity is identically zero (yellow) between the source and the receiver-to-source caustic, $0^\circ < \phi < 20^\circ$, and between the receiver and the source-to-receiver caustic, $40^\circ < \phi < 60^\circ$, whereas it is minimal (red) between the two caustics, $20^\circ < \phi < 40^\circ$. These differences are produced by the jumps in the source-to-scatterer and receiver-to-scatterer Maslov indices:

$$M' + M'' - M = \begin{cases} 0 & \text{if } 0^\circ < \phi < 20^\circ \\ -1 & \text{if } 20^\circ < \phi < 40^\circ \\ 0 & \text{if } 40^\circ < \phi < 60^\circ \end{cases} . \tag{51}$$

The oscillatory term in the numerator of (21) changes character as a result of these jumps,

$$\begin{aligned} &\sin\omega(T' + T'' - T) \to \cos\omega(T' + T'' - T) \\ &\quad \to \sin\omega(T' + T'' - T) , \end{aligned} \tag{52}$$

as we move along, or very nearly along, the ray from the source **s** to the receiver **r**.

In Fig. 13(b) we display a series of quasi-perpendicular cross-sections of the kernel K_c, at equally spaced longitudes

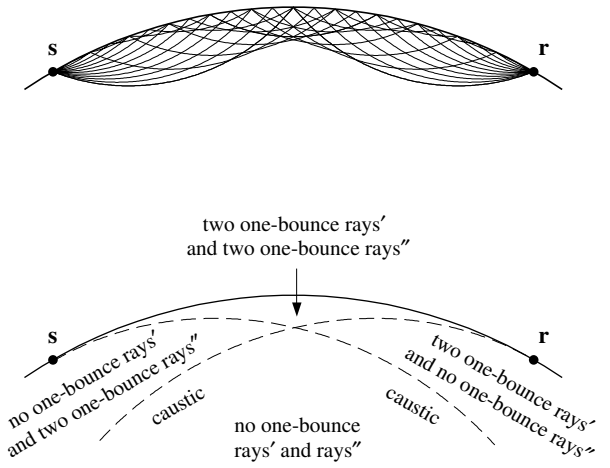

Figure 10. (Top) Family of *PP* rays shot from a surface source **s** and receiver **r**. The source-to-receiver and receiver-to-source caustics are the loci where adjacent rays cross. (Bottom) Dashed lines tangent to the surface of the earth at **s** and **r** denote these two bowl-shaped caustic surfaces. The caustics subdivide the space of single scatterers **x** into four regions, as shown.

$\phi = 30°$, 35°, 40°, 45°, 50°, 55°; in Fig. 13(c) we show several constant-depth slices at $h = 20$, 100, 200, 400 km; and in Fig. 13(d) we show a number of vertical slices parallel to the ray plane, at colatitudes $90° \pm 1°$, $90° \pm 2°$, $90° \pm 3°$. The traveltime sensitivity is essentially zero (yellow) at all points **x** situated below the source-to-receiver and the receiver-to-source caustics, because no like-type (single surface reflection) rays′ or rays″ can be traced from **s** or **r** to this region of 'scatterer space', as discussed above. The $\phi = 40°$ section passes directly through the caustic; the saturated 'red-brick' character of K_c expresses the strong sensitivity of a *PP* traveltime shift δT to wave-speed heterogeneity $\delta c/c$ at this point. The saddle-shaped character of the near-surface depth slices, $h = 20$, 100 km, is a consequence of the minimax nature of the *PP* wave. Waves that scatter off in-plane heterogeneity $\delta c/c$ to the 'east' or 'west' of the surface bounce point $\phi = 30°$ travel deeper and therefore arrive earlier than the geometrical *PP* wave, whereas those that scatter off heterogeneity to the 'north' or 'south' take an out-of-plane detour and therefore arrive later than the *PP* wave. At deeper depths, $h = 200$ km, it becomes evident that there are in reality two saddles, one with its 'stirrups' dipping towards the ray plane and the other with them dipping away.

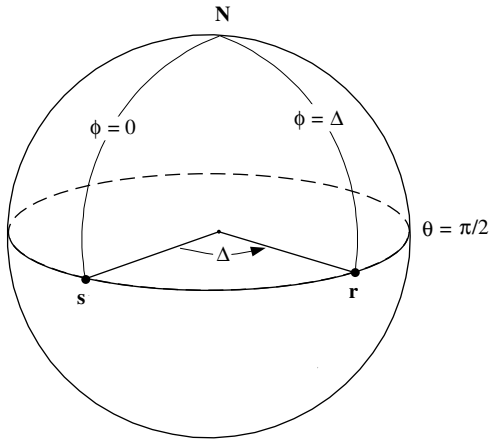

Figure 11. Schematic depiction of the equatorial coordinate system used to depict the 'exact' and paraxial Fréchet kernels K_c and K. The North Pole is denoted by N.

In summary, the traveltime Fréchet kernel of a *PP* or *SS* wave is a wondrously shaggy 3-D beast, characterized by strong positive ($K_c > 0$) as well as negative ($K_c < 0$) sensitivity to off-path wave-speed heterogeneity far away from the geometrical ray. In most contemporary tomographic studies, this complicated 3-D dependence upon $\delta c/c$ is replaced by a 1-D line integral (35) along the ray. Even more crudely, a measured traveltime shift δT_{PP} or δT_{SS} is often considered to be a vertically averaged, near-surface advance or delay accumulated just beneath the surface reflection point. It is evident from Fig. 13 that any such pointwise interpretation is a considerable approximation!

4.3 *PcP* wave

The traveltimes of single *PcP* and *ScS* core reflections and multiple PcP_2, PcP_3, ... and ScS_2, ScS_3, ... reverberations provide another rich source of tomographic data, which can be used to constrain mantle heterogeneity in the corridor between a source **s** and a receiver **r** (e.g. Sipkin & Jordan 1976, 1980; Katzman *et al.* 1998). Fig. 14 shows the 3-D Fréchet kernel K_c of a $\tau = 20$ s *PcP* wave, recorded at an epicentral distance $\Delta = 44°$. In essence, K_c is a hollow banana that is folded over itself at the core reflection point, $\phi = 22°$. The ray-plane ($\theta = 90°$) cross-section is depicted in Fig. 14(a); the black curve shows the depth variation of the sensitivity along a line through the reflection point. Fig. 14(b) shows two longitudinal slices, at $\phi = 22°$ and $\phi = 33°$, and Fig. 14(c) shows four depth slices, at $h = 2850$, $h = 2800$, $h = 2700$ and $h = 2500$ km. The maximum sensitivity is not located right on the core–mantle boundary, at a depth $h = 2900$ km, but rather at the 'cross-over point' of the folded banana skins, approximately 200–250 km above. The interior 'fissioning doughnut' is due to the constructive interference of like-type scattered waves within the first Fresnel zone; however, the fringing green and red ellipses are the result of unlike-type *P*-to-*P* scattering paths, which happen to have a traveltime $T' + T''$ similar to the time T of the *PcP* wave. The bowl-shaped locus of these *P*-to-*P* scatterers **x** is barely visible—try squinting—in Fig. 14(a). The final view, Fig. 14(d), shows the off-path structure on a series of colatitudinal slices, at $90° \pm 1°$, $90° \pm 2°$ and $90° \pm 3°$.

5 PARAXIAL APPROXIMATION

In the above three examples, as well as all other cases we have investigated, the dominant contribution to the 'exact' traveltime kernels K_c comes from like-type forward-scattering ($\hat{\mathbf{k}}'' \approx \hat{\mathbf{k}}'$) paths in the vicinity of the unperturbed ray path. An unlike-type composite path is a forward-and-backward pair ray′, ray″ that does not have the same total number of surface and core–mantle boundary reflections as the central ray. These make relatively minor contributions to the double sum (18) in only two situations.

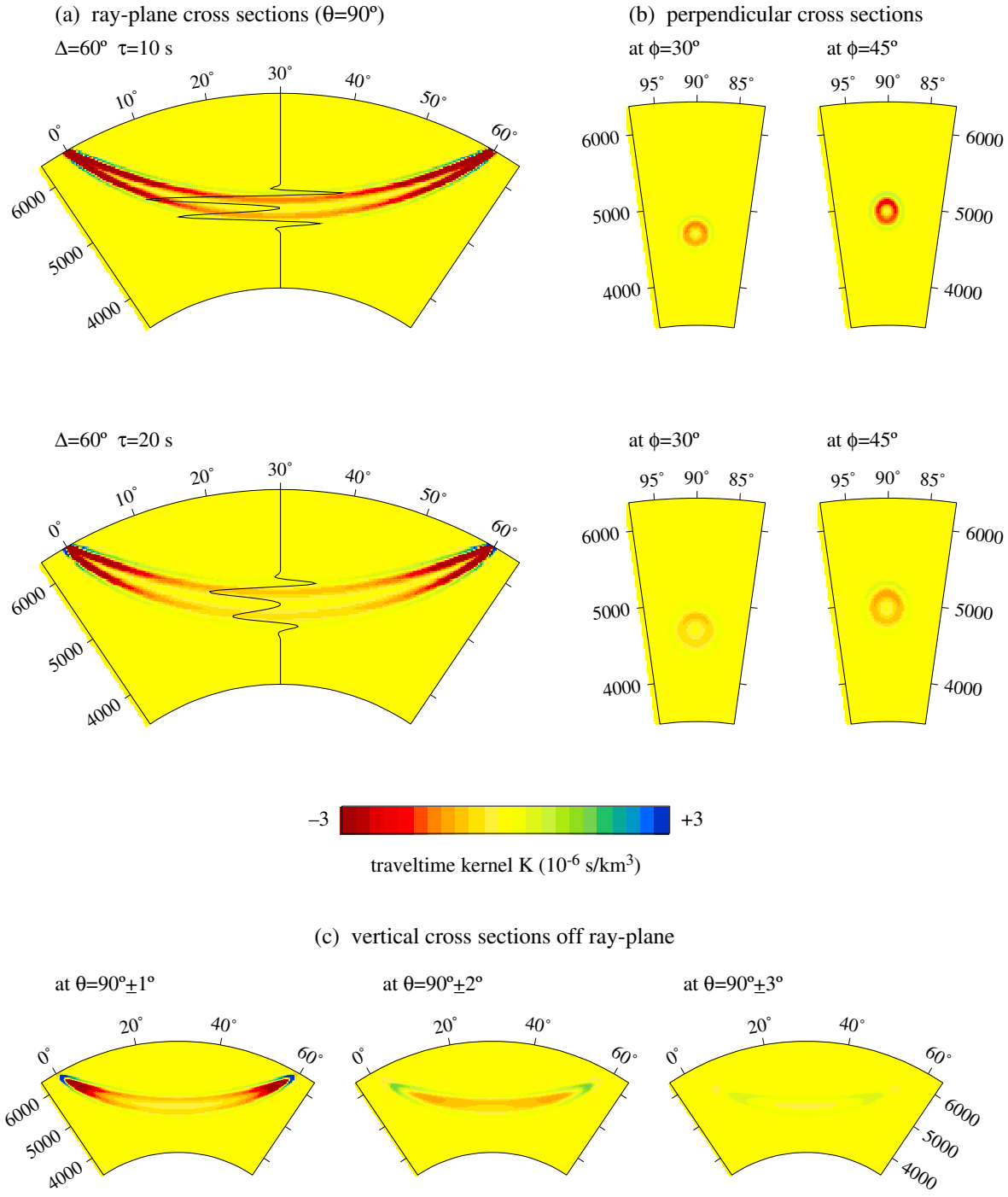

Figure 12. 2-D cross-sections through the 3-D 'exact' Fréchet kernel K_c for a teleseismic P wave at an epicentral distance $\Delta = 60^\circ$. (a) Ray-plane cross-sections; solid lines show the variation of K_c with depth on a line through the turning point. (b) Longitudinal cross-sections at $\phi = 30^\circ$ and $\phi = 45^\circ$. Top panel shows the kernel for a $\tau = 10$ s wave and bottom panel shows the kernel for a $\tau = 20$ s wave in both cases. (c) Vertical cross-sections through the $\tau = 20$ s kernel at distances $\pm 1^\circ$, $\pm 2^\circ$ and $\pm 3^\circ$ off the ray plane.

(1) At points **x** in the vicinity of a surface reflection point, the direct source-to-scatterer-to-receiver traveltime $T' + T''$ can be very nearly equal to the reflection time T. This gives rise to small modifications in the kernels K_c of reflected phases such as *PP* and *PcP* in thin 'boundary layers' near the reflecting boundaries.

(2) In addition, there may be occasional 'accidental' traveltime coincidences $T' + T'' \approx T$ such as the one that gives rise to the nearly invisible bowl-shaped flange on the *PcP*-wave kernel in Figs 14(a) and (c).

Both of these effects are ignored in the paraxial approximation (26)–(28). We investigate the veracity of this approximation by comparing the paraxial kernels K for a P, PP and PcP wave with the corresponding 'exact' kernels K_c in this section.

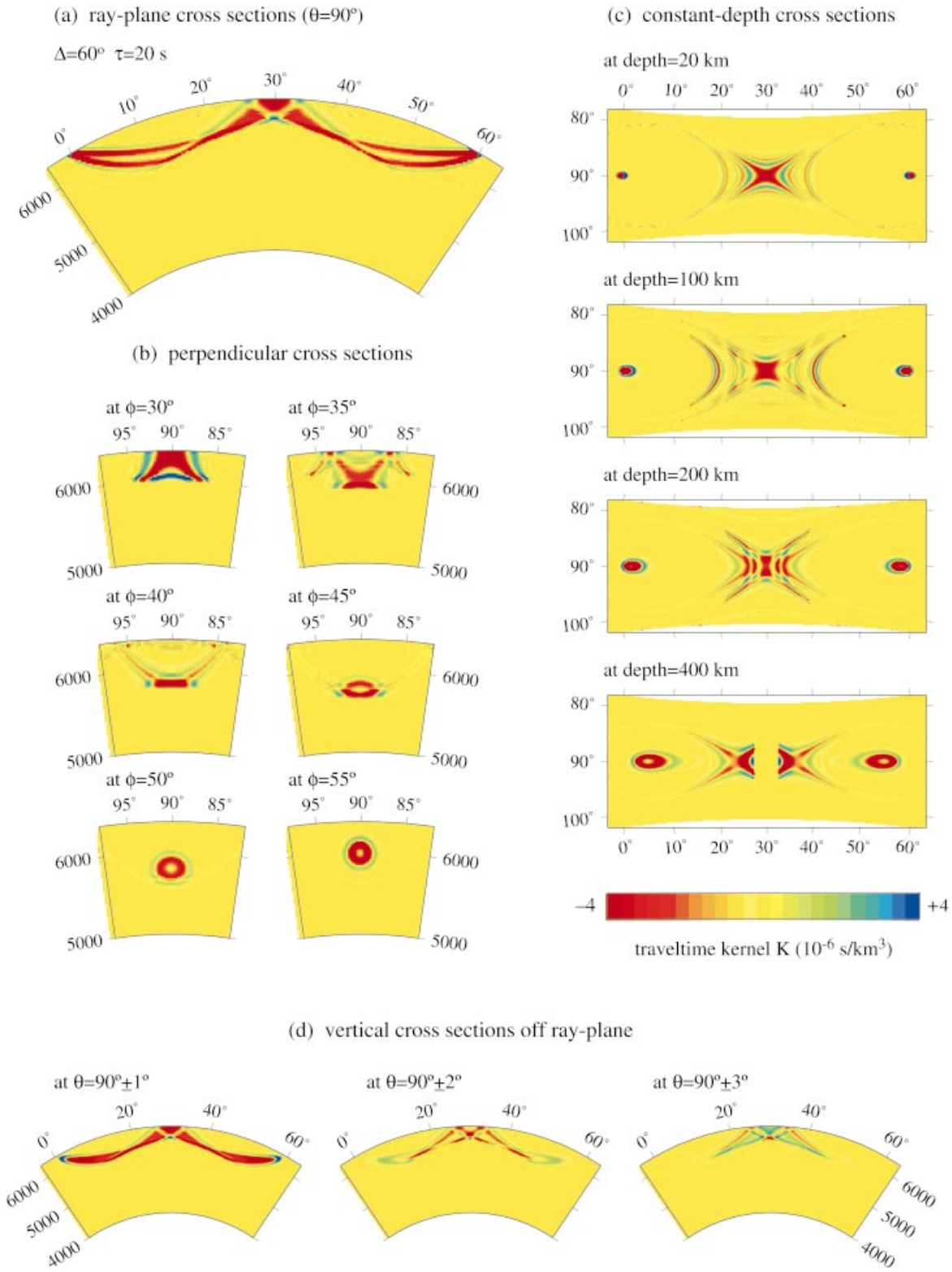

Figure 13. 2-D cross-sections through the 3-D 'exact' Fréchet kernel K_c for a minimax *PP* wave, with a characteristic period $\tau = 20$ s at an epicentral distance $\Delta = 60°$. (a) Ray-plane slice at $\theta = 90°$. (b) Longitudinal slices at $\phi = 30°, 35°, 40°, 45°, 50°, 55°$. (c) Constant-depth slices at $h = 20, 100, 200, 400$ km; the corresponding radii are $r = 6351, 6271, 6171, 5971$ km. (d) Vertical slices at distances $\pm 1°, \pm 2°, \pm 3°$ off the ray plane.

5.1 *P* wave

Fig. 15 shows the paraxial Fréchet kernel K for a $\tau = 10$ s and a $\tau = 20$ s *P* wave at an angular epicentral distance $\Delta = 60°$. The source–receiver geometry, all of the cross-sectional views, the plotting format and the colour scale are all identical to those in Fig. 12. It is evident that the agreement between the 'exact' and approximate kernels is excellent. The construction of the

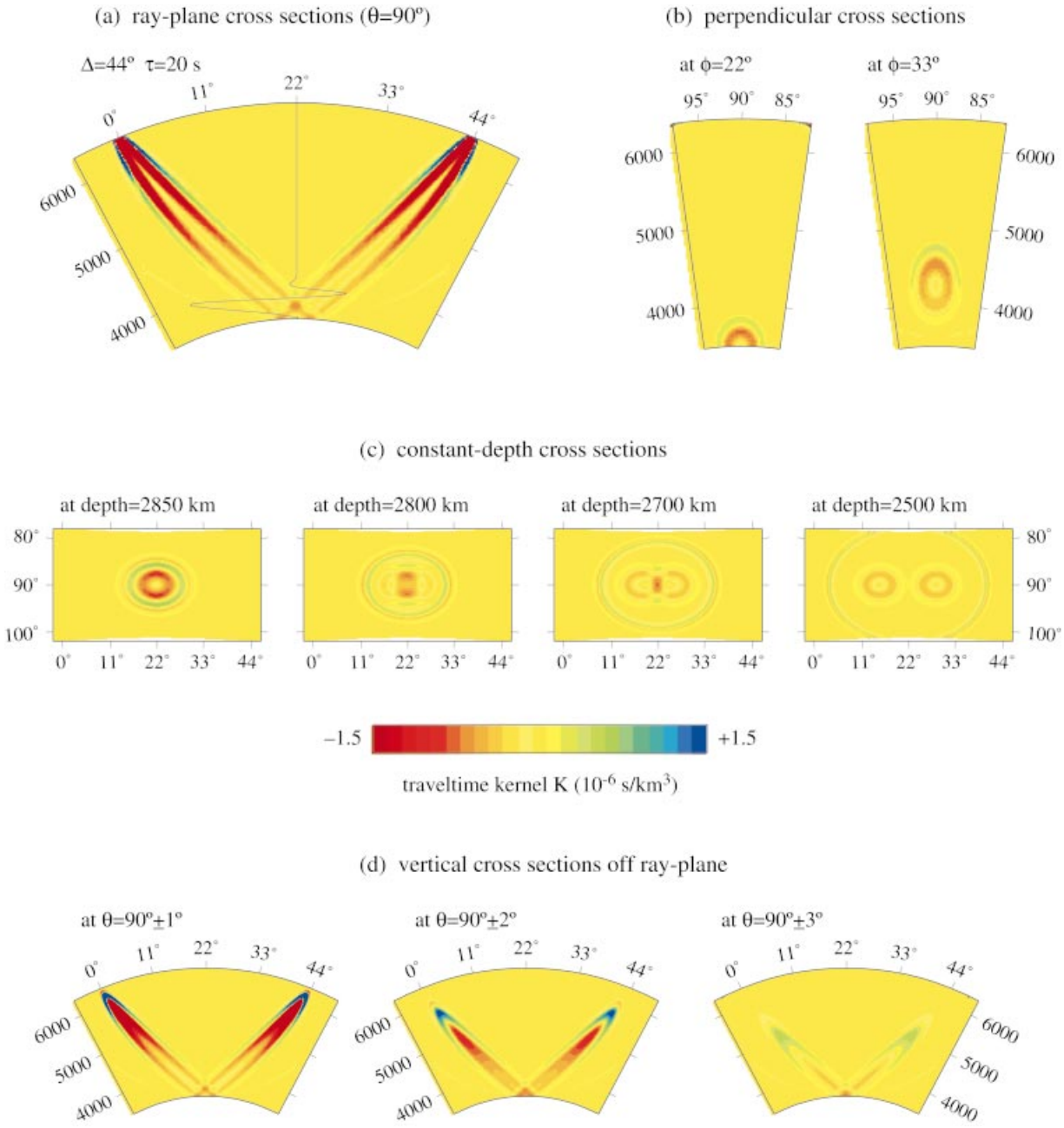

Figure 14. 2-D cross-sections through the 3-D 'exact' Fréchet kernel K_c for a $\tau = 20$ s *PcP* wave at an epicentral distance $\Delta = 44°$. (a) Ray-plane cross-section at $\theta = 90°$; black curve shows the depth variation of K_c on a plumb line through the CMB bounce point. (b) Longitudinal cross-sections at $\phi = 22°$, 33°. (c) Constant-depth cross-sections at $h = 2850$, 2800, 2700, 2500 km (i.e. 50, 100, 200, 400 km above the core–mantle boundary). (d) Vertical cross-sections at distances $\pm 1°$, $\pm 2°$, $\pm 3°$ off the ray plane.

paraxial kernel K of a P wave is extremely straightforward—every scatterer $\mathbf{x}$ is projected onto a single point $\boldsymbol{\xi}$ on the central source-to-receiver ray.

It is immaterial in the context of the paraxial approximation whether the leading factor of c in eq. (27) is evaluated at the position of the scatterer $\mathbf{x}$ or at the projection point $\boldsymbol{\xi}$. The former alternative is preferable, because it leads to a better agreement between the paraxial and 'exact' kernels K and K_c. In particular, the slightly larger sensitivity in the uppermost banana 'skin' is more accurately reproduced. This subtle difference between the upper and lower sensitivities may be most easily seen by comparing the black curves, showing the radial dependence of K and K_c along a line through the turning point. The slightly darker red and fringing green at the top of the doughnut cross-sections in Figs 15(b) and 12(b) is also evident. If $c(\mathbf{x})$ were replaced by $c(\boldsymbol{\xi})$ in eq. (27), the paraxial doughnut would be circularly symmetric.

5.2 *PP* wave

In Fig. 16, we illustrate the paraxial traveltime kernel K for a $\tau = 20$ s *PP* wave at an epicentral distance $\Delta = 60°$ for comparison with Fig. 13. In this case, every scatterer $\mathbf{x}$ must be projected onto two points $\boldsymbol{\xi}$, one on each leg of the

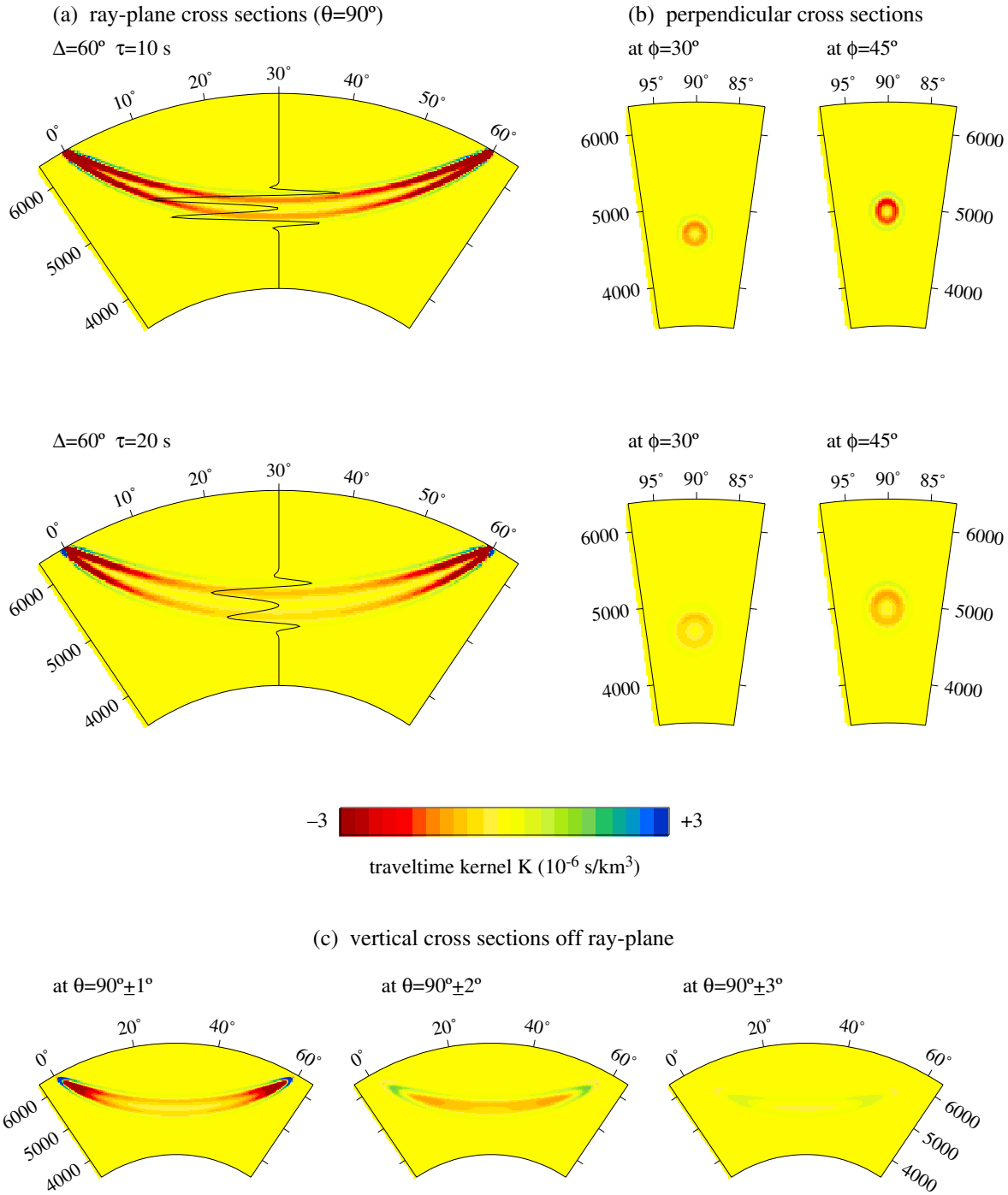

Figure 15. 2-D cross-sections through the 3-D paraxial Fréchet kernel K for a teleseismic P wave at an epicentral distance $\Delta = 60^\circ$. Compare with the corresponding views of the 'exact' kernel K_c in Fig. 12.

central geometrical ray. The sum of forward and backward traveltime Hessians $\mathbf{M}' + \mathbf{M}''$ is divergent at both the source-to-receiver and receiver-to-source caustics, $\phi = 2\Delta/3 = 40^\circ$ and $\phi = \Delta/3 = 20^\circ$, as we discuss in Appendix A5. The associated jump discontinuities in the signature,

$$\operatorname{sig}(\mathbf{M}' + \mathbf{M}'') = \begin{cases} 2 & \text{if } 0^\circ < \phi < 20^\circ \\ 0 & \text{if } 20^\circ < \phi < 40^\circ \\ 2 & \text{if } 40^\circ < \phi < 60^\circ \end{cases}, \tag{53}$$

are responsible for the characteristic zero-to-maximal-to-zero sensitivity variations (51) along the ray:

$$\sin \frac{1}{2}\,\omega \mathbf{q}^{\mathrm{T}} \cdot (\mathbf{M}' + \mathbf{M}'') \cdot \mathbf{q} \to \cos \frac{1}{2}\,\omega \mathbf{q}^{\mathrm{T}} \cdot (\mathbf{M}' + \mathbf{M}'') \cdot \mathbf{q}$$

$$\to \sin \frac{1}{2}\,\omega \mathbf{q}^{\mathrm{T}} \cdot (\mathbf{M}' + \mathbf{M}'') \cdot \mathbf{q}\,. \tag{54}$$

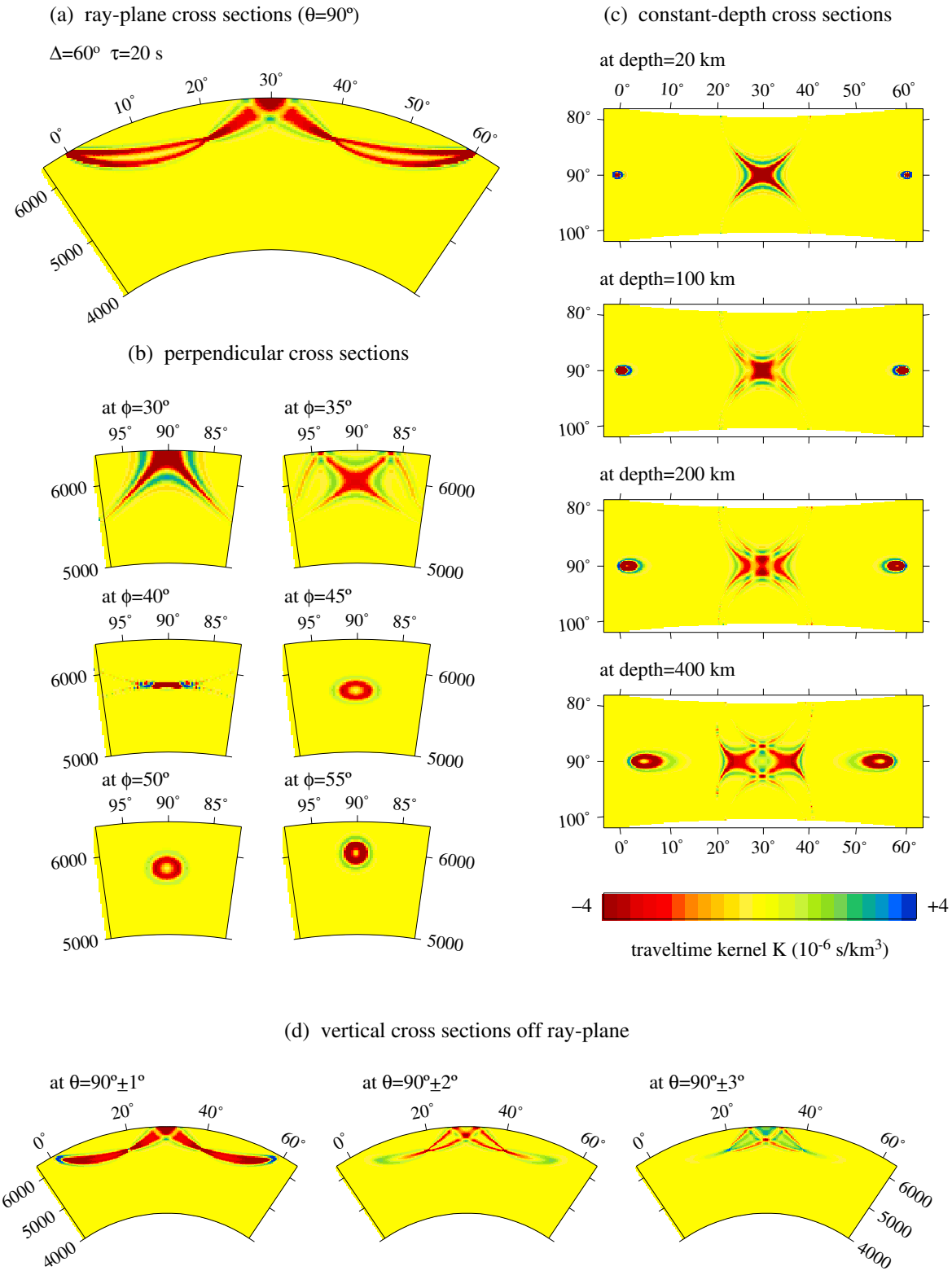

Figure 16. 2-D cross-sections through the 3-D paraxial Fréchet kernel K for a *PP* wave at an epicentral distance $\Delta = 60°$. Compare with the corresponding views of the 'exact' kernel K_c in Fig. 13.

The in-plane variation of the paraxial kernel (27)–(28) in the vicinity of the two caustics is extremely singular:

$$K \sim \begin{cases} -\dfrac{\sqrt{\infty}}{2\pi c} \dfrac{\displaystyle\int_0^\infty \omega^3 |\dot{m}(\omega)|^2 \sin \frac{1}{2} \infty \omega q_1^2 \, d\omega}{\displaystyle\int_0^\infty \omega^2 |\dot{m}(\omega)|^2 \, d\omega} & \phi\uparrow 20^\circ,\ \phi\downarrow 40^\circ \\ -\dfrac{\sqrt{\infty}}{2\pi c} \dfrac{\displaystyle\int_0^\infty \omega^3 |\dot{m}(\omega)|^2 \cos \frac{1}{2} \infty \omega q_1^2 \, d\omega}{\displaystyle\int_0^\infty \omega^2 |\dot{m}(\omega)|^2 \, d\omega} & \phi\downarrow 20^\circ,\ \phi\uparrow 40^\circ \end{cases}, \tag{55}$$

where $\uparrow$ and $\downarrow$ specify whether the caustics are approached from the source or receiver side, respectively. The leading factor of $\sqrt{\infty}$ in (55) renders the traveltime shift δT_{PP} very sensitive to heterogeneity δc in the vicinity of the two caustics; however, the infinitely oscillatory terms shrink the width of the paraxial kernel to zero at these points, as illustrated in Fig. 16(a).

In general, the paraxial *PP* kernel K is in very good agreement with the 'exact' kernel K_c. The principal discrepancies occur in the vicinity of the source-to-receiver and receiver-to-source caustics, and in a thin boundary layer near the upper surface of the earth, particularly in the tails of the saddle. Most of these discrepancies are due to the neglect of unlike-type scattering paths; for example, at scatterers **x** near the surface reflection point, both no-bounce *P*-to-*P* and two-bounce *Pp*-to-*pP* rays contribute to K_c but not to K. The 'swallowtails' extending down into the earth, beneath $r = 6000$ km, in the perpendicular cross-sections at $\phi = 30^\circ$ and $\phi = 35^\circ$ in Fig. 16(b) are another clear difference. The 'exact' kernel K_c in Fig. 13(b) is essentially zero at all scatterers **x** beneath the two caustic surfaces, as we have seen.

5.3 *PcP* wave

Fig. 17 shows the paraxial kernel K for a $\tau = 20$ s *PcP* wave at an epicentral distance $\Delta = 44^\circ$; every scatterer is again projected onto two points $\boldsymbol{\xi}$, one on each leg of the compound ray. The agreement with the 'exact' wave-speed kernel K_c depicted in Fig. 14 is seen to be excellent. Close inspection reveals a slight discrepancy in the vicinity of the core–mantle boundary reflection point, where no-bounce *P*-to-*P* and two-bounce *PcP*-to-*PcP* scattering paths contribute to K_c, but not to K. The bowl-shaped flange in Figs 14(a) and (c) is also absent in Figs 17(a) and (c), as noted previously.

6 DIFFERENTIAL KERNEL

Differential traveltime shifts $\delta(\Delta T)$ are widely used in both global and regional tomographic studies because they are thought to be particularly sensitive to wave-speed variations δc in a particular region within the earth. For example, the relative traveltime variations of teleseismic *P* waves at a number of closely spaced stations are frequently used to invert for the wave-speed heterogeneity δc beneath a seismic network or array; the effect of near-source and deep-mantle anomalies δc is considered to be negligible, because those portions of the associated ray paths are virtually identical (e.g. Aki *et al.* 1977; Humphreys *et al.* 1984; VanDecar & Crosson 1990). Differential *PP–P* and *SS–S* traveltime shifts at a single station are likewise often ascribed to heterogeneity δc in the vicinity of the surface reflection, on the grounds that the near-source and near-receiver ray paths are similar (e.g. Kuo *et al.* 1987; Sheehan & Solomon 1991; Woodward & Masters 1991). Another popular single-station technique makes use of differential traveltime shifts between successive multiple *PcP* or *ScS* reverberations; a sequence PcP_2–PcP_1, PcP_3–PcP_2, ... or ScS_2–ScS_1, ScS_3–ScS_2, ... of such measurements can be used to constrain the heterogeneity δc in a 2-D corridor between a source **s** and receiver **r** (e.g. Sipkin & Jordan 1980; Katzman *et al.* 1998). We present a number of 3-D Fréchet kernels $K^{B-A} = K^B - K^A$ for such differential traveltime measurements $\delta(T_B - T_A)$ in Fig. 18; all of the illustrated differential kernels have been computed using the identical-pulse-shape paraxial approximation (33)–(34).

The left side of Fig. 18(a) shows a ray-plane cross-section of the paraxial sensitivity kernel for a differential traveltime measurement made by cross-correlating two $\tau = 20$ s *P* waves, recorded at a pair of closely spaced stations situated on the same azimuth, at epicentral distances $\Delta = 61^\circ$ and $\Delta = 60^\circ$. The sensitivity is very slight over the first two-thirds of the ray path, $0^\circ < \phi < 40^\circ$, as expected. The Fresnel zones of the individual waves overlap beneath the array; the red and blue banana 'skins' delineate the maximum sensitivity of the 61° and 60° arrivals, respectively. These two regions of maximal sensitivity are of opposite sign, since the measured quantity is the shift in the traveltime *difference* $\delta(T_{61^\circ} - T_{60^\circ})$. In the ray-theoretical limit, the kernel would consist of a single red and a single blue 'spaghetti stalk', one along each of the constituent rays.

The right side of Fig. 18(a) shows the ray-plane sensitivity of a $\tau = 20$ s *PP–P* differential traveltime measurement, at an epicentral distance $\Delta = 60^\circ$. The 3-D Fréchet kernel is simply the difference of the *PP* and *P* kernels: $K^{PP-P} = K^{PP} - K^P$. Near-source and near-receiver heterogeneity δc whose lateral scale is wider than about 5° will tend to be cancelled by the rapidly alternating zones of red and blue sensitivity; however, heterogeneity that is significantly narrower than this may not be subject to this cancellation. Kernels analogous to those in Fig. 18(a) were presented by Marquering *et al.* (1999). Their differential kernels, which are computed by means of surface wave summation, are very similar to those shown here.

Figs 18(b) and (c) depict a sequence of kernels for the differential traveltimes of $\tau = 20$ s PcP_2–PcP_1, PcP_3–PcP_2 and PcP_4–PcP_3 waves, at an epicentral distance $\Delta = 48^\circ$. The finite-frequency sensitivity of these low-ray-parameter waves *cannot* be computed by surface wave summation. The maximum ray-plane sensitivity in each panel of Fig. 18(b) is in the vicinity of the source **s** and the receiver **r**. As in the case of *PP–P*, the alternating red and blue zones of sensitivity will tend to cancel the effect of *sufficiently smooth* subsource and subreceiver heterogeneity δc. The intensity of the alternating zones decreases from left (PcP_2–PcP_1) to right (PcP_4–PcP_3), showing that the cancellation effect is more pronounced for the more steeply incident waves, whose near-source and near-receiver geometrical ray paths are closer together. The alternating zones of negative (orange) and positive (green) sensitivity in the upper mantle are indicative of the degree of lateral coverage and resolution in the source-to-receiver corridor. It is noteworthy that these shallow minima and maxima are *not* centred

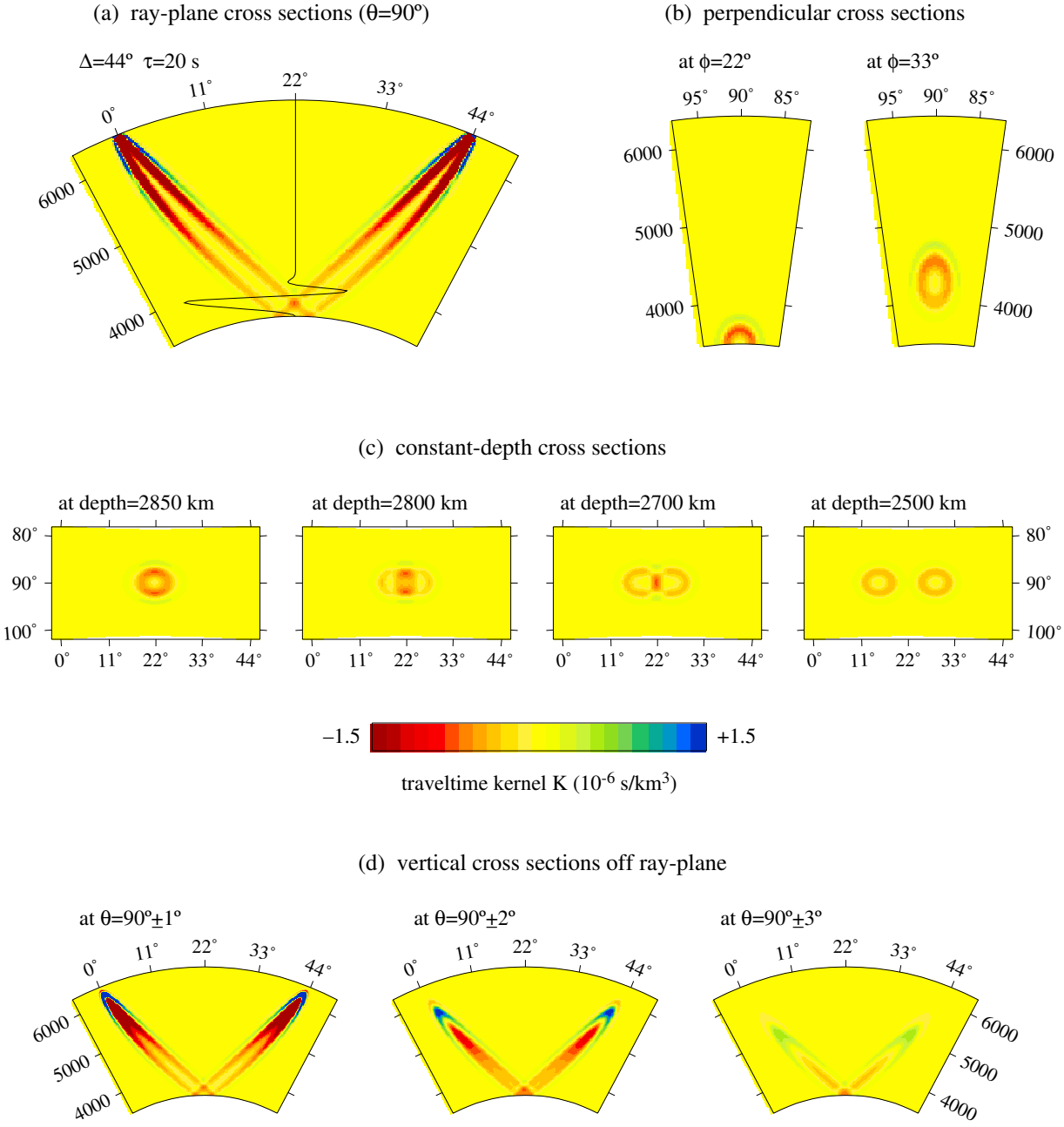

Figure 17. 2-D cross-sections through the 3-D paraxial Fréchet kernel K for a *PcP* wave at an epicentral distance $\Delta = 44°$. Compare with the corresponding views of the 'exact' kernel K_c in Fig. 14.

upon the surface reflection points—for the same reason that a single-phase kernel is a *hollow* banana. The off-path sensitivity at a depth $h = 400$ km extends to $\pm 5°$, as illustrated in Fig. 18(c). As we have noted earlier, this cross-path width scales as the square root $\sqrt{\tau}$ of the characteristic period of the cross-correlated waves.

In a recent tomographic study, Katzman *et al.* (1998) used 2-D multiple-ScS_{SH} Fréchet kernels K^{2D}, computed by Zhao & Jordan (1998) by means of whole-earth normal-mode summation, to image the heterogeneity in upper mantle shear wave speed along a corridor between Tonga and Hawaii. Such 2-D traveltime kernels are appropriate only if the heterogeneity is cylindrically symmetric or quasi-symmetric in the cross-path direction (Marquering *et al.* 1999). A 3-D rather than 2-D analysis of the Tonga–Hawaii corridor might lead to different conclusions, inasmuch as the kernels K and K^{2D} are fundamentally different—most notably, the latter do *not* exhibit zero sensitivity along the geometrical ray.

7 DEPTH PHASE INTERFERENCE

In all of the examples presented so far in this paper, the various phases examined, *P*, *PP*, *PcP*, PcP_2, ..., have been

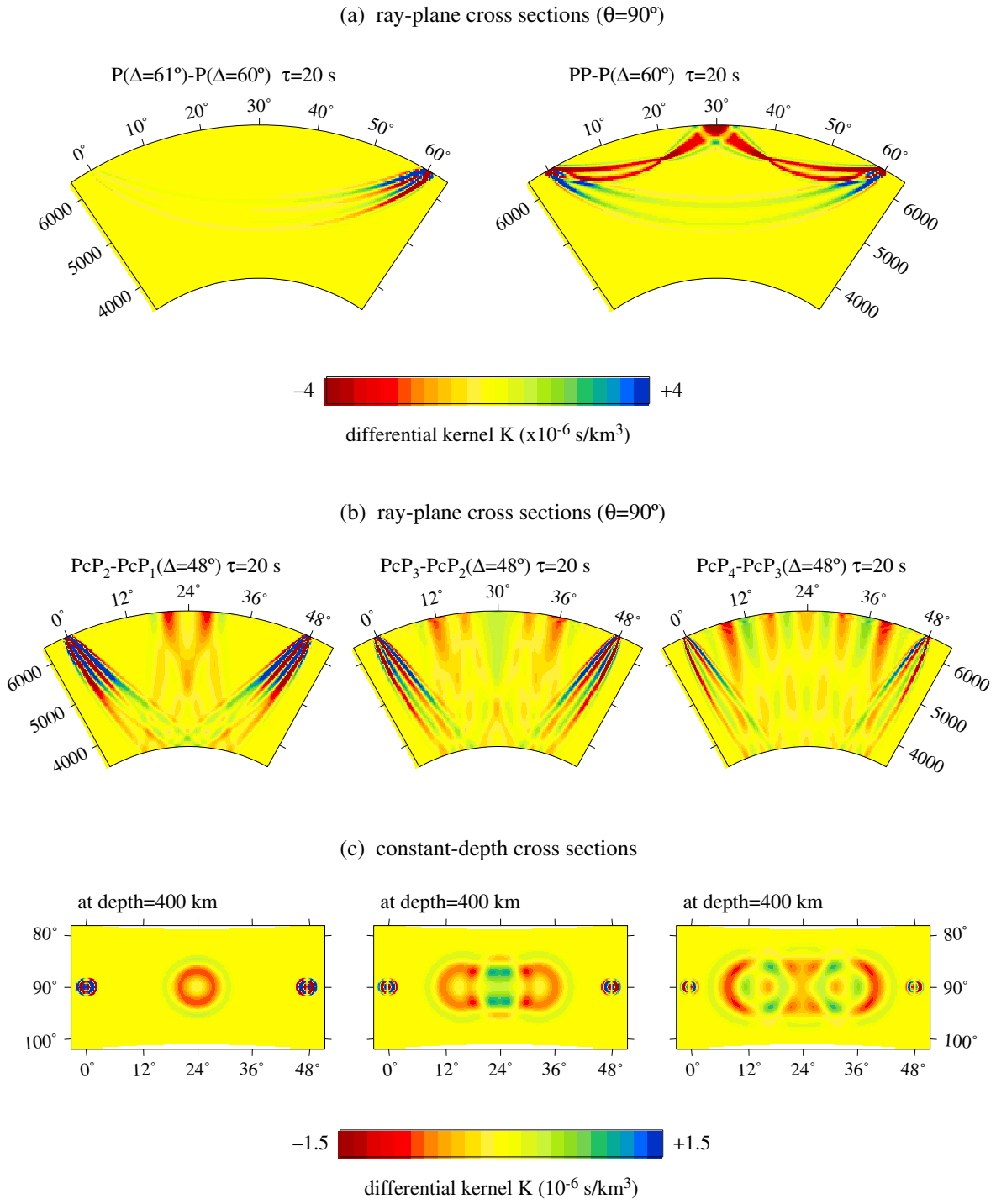

Figure 18. Differential traveltime kernels for $\tau = 20$ s waves computed using the paraxial approximation. (a) (Left) Ray-plane cross-section showing the sensitivity of the differential P-wave traveltime between two stations, located on the same azimuth, at epicentral distances $\Delta = 60^\circ$ and $\Delta = 61^\circ$. (Right) Sensitivity of a *PP–P* differential traveltime measurement at an epicentral distance $\Delta = 60^\circ$. (b) Ray-plane cross-sections showing the sensitivity of PcP_2–PcP_1, PcP_3–PcP_2 and PcP_4–PcP_3 differential traveltime measurements at an epicentral distance $\Delta = 48^\circ$. (c) Upper-mantle ($h = 400$ km, $r = 5971$ km) constant-depth slices for the same PcP_2–PcP_1, PcP_3–PcP_2 and PcP_4–PcP_3 differential traveltimes.

well separated in the time domain. In a more complicated earth model, with a Mohorovičić or other internal discontinuities, there may be more than one significant body wave phase that arrives within the cross-correlation time interval $t_1 \le t \le t_2$. We develop a general procedure that can be used to construct 3-D Fréchet kernels for such interfering or overlapping phases in Banana–Doughnut I. To illustrate this extended theory, we consider an especially simple case here.

Thus far, the explosive source **s** has been situated upon the earth's surface; we now suppose that it is *buried*, at a depth d. The direct P wave at a distant station will in that case be followed by the surface reflection pP. For a sufficiently shallow source, the pP–P traveltime difference may be short compared to the characteristic period of the wave, $T_{pP}-T_P \approx 2d/c_0 < \tau$; in that case the two phases will interfere.

7.1 Recapitulation

We show in Banana–Doughnut I that the paraxial Fréchet kernel for the two superimposed phases is a sum of four terms that account for the influence of P and pP scattered waves upon the traveltimes of the unperturbed P and pP pulses, respectively:

$$\begin{aligned} K_{P+pP} = &-\frac{1}{2\pi c D}\int_0^\infty \omega^3 |\dot m(\omega)|^2 \\ &\times [\mathscr{R}_P^{-2}\sqrt{|\det(\mathbf{M}'_P+\mathbf{M}''_P)|}\,\sin\omega\,\Delta T_P \\ &+\mathscr{R}_P^{-1}\mathscr{R}_{pP}^{-1}\sqrt{|\det(\mathbf{M}'_P+\mathbf{M}''_P)|}\,\sin\omega\,(\Delta T_P + T_P - T_{pP}) \\ &+\mathscr{R}_{pP}^{-1}\mathscr{R}_P^{-1}\sqrt{|\det(\mathbf{M}'_{pP}+\mathbf{M}''_{pP})|}\,\sin\omega\,(\Delta T_{pP} + T_{pP} - T_P) \\ &+\mathscr{R}_{pP}^{-2}\sqrt{|\det(\mathbf{M}'_{pP}+\mathbf{M}''_{pP})|}\,\sin\omega\,\Delta T_{pP}]\,d\omega\,, \end{aligned} \tag{56}$$

where

$$\Delta T_P = \frac{1}{2}\,\mathbf{q}^{\mathrm{T}}\cdot(\mathbf{M}'_P+\mathbf{M}''_P)\cdot\mathbf{q}\,, \tag{57}$$

$$\Delta T_{pP} = \frac{1}{2}\,\mathbf{q}^{\mathrm{T}}\cdot(\mathbf{M}'_{pP}+\mathbf{M}''_{pP})\cdot\mathbf{q} \tag{58}$$

and

$$D = \int_0^\infty \omega^2|\dot m(\omega)|^2[\mathscr{R}_P^{-2}+\mathscr{R}_{pP}^{-2}+2\mathscr{R}_P^{-1}\mathscr{R}_{pP}^{-1}\cos\omega(T_P-T_{pP})]\,d\omega\,. \tag{59}$$

The subscripts on the central-ray traveltimes T_P, T_{pP} and the forward and backward Hessians $\mathbf{M}'_P$, $\mathbf{M}''_P$, $\mathbf{M}'_{pP}$, $\mathbf{M}''_{pP}$ specify the two interfering phases. The amplitude factors A_P and A_{pP} cancel, since they are identical.

In the limit of a surface-focus source, $d\to 0$, the two phases have the same traveltimes and geometrical spreading factors:

$$T_P = T_{pP}\,, \qquad \mathscr{R}_P = \mathscr{R}_{pP}\,. \tag{60}$$

The kernel (56) then reduces to that for either of the phases considered individually:

$$K_{P+pP} = K_P = K_{pP}\,. \tag{61}$$

In the opposite limit of a very deep source, $T_{pP}-T_P \gg \tau$, the two arrivals will be well separated in time; the multiphase kernel (56) in that case reduces to a sum of individual kernels, each weighted by the relative (amplitude)^2 of the associated pulse:

$$K_{P+pP} = \left(\frac{\mathscr{R}_P^{-2}}{\mathscr{R}_P^{-2}+\mathscr{R}_P^{-2}}\right)K_P + \left(\frac{\mathscr{R}_{pP}^{-2}}{\mathscr{R}_P^{-2}+\mathscr{R}_{pP}^{-2}}\right)K_{pP}\,. \tag{62}$$

In practice, the deep-source limit (62) is not of great interest; whenever the direct and depth phases are well separated, it is obviously preferable to measure the individual time-shifts δT_P and δT_{pP}.

7.2 $P+pP$ Fréchet kernel

Fig. 19 compares the Fr echet kernels K_{P+pP} for four buried sources **s**, at depths $d=5$, 10, 15, 20 km. The receiver **r** is situated on the surface, at an epicentral distance $\Delta=60^\circ$; the characteristic period is $\tau=20$ s. The black curves on the ray-plane cross-sections show the variation of the sensitivity as a function of depth along a line at the turning point for a surface source, $\phi=30^\circ$. The synthetic waveforms $p_P(t)+p_{pP}(t)$ at **r** are depicted to the right of each kernel cross-section; the later-arriving pP phase moves out with respect to P as the source depth is increased. For the shallowest ($d=5$ km) source, the waveform is essentially indistinguishable from a single pulse; the amplitude is approximately twice that of an isolated P or pP phase, due to the nearly simultaneous arrival. Despite the rather severe distortion of the pulse shapes for the deeper ($d=10$–20 km) sources, the kernels K_{P+pP} exhibit relatively modest perturbations. There are slight changes in the outer fringing Fresnel zones because of phase interference and adjacent-path scattering effects; however, the gross banana–doughnut character is retained. Note, in particular, that the sensitivity is nearly zero (yellow) in the vicinity of the P and pP ray paths, and negative (red) in the surrounding banana skin. We are encouraged by this preliminary result to think that phase interference might not be an important effect in more complicated, realistic earth models—although we recognize that this presumption needs to be much more extensively tested. Many other possibly problematical examples come to mind; for example, what is the effect of precursory underside reflections off the Mohorovičić discontinuity upon the kernel of a PP or SS wave?

8 CONCLUSIONS

Two important conclusions can be drawn from the preliminary comparison with 'ground-truth' pseudospectral synthetic seismograms and the illustrative examples of absolute and differential traveltime sensitivity kernels presented in this paper. First, 3-D Born–Fréchet kernel theory does an excellent job of modelling finite-frequency traveltime shifts measured by cross-correlation. Second, the paraxial kernel K is an excellent approximation to the 'exact' ray-theoretical kernel K_c. Geometrical ray theory provides an adequate basis for seismic traveltime tomography only if the cross-path scale length of the wave-speed heterogeneity δc is much greater than the width of the banana–doughnut kernel K. Absolute and differential cross-correlation traveltimes are often measured using intermediate-period and long-period waves, which have wavelengths of the order of 100–1000 km. Contemporary models of the compressional and shear wave speeds within the mantle exhibit variations with comparable scale lengths (Grand *et al.* 1997). It is evident that future attempts to resolve even finer-scale detail must go beyond ray theory. We have shown in the Appendix to Banana–Doughnut I that it is extremely economical to compute the paraxial kernel K in a realistic spherically symmetric earth model. The way is now open to the exploitation of 3-D Fréchet kernels in global traveltime tomography.

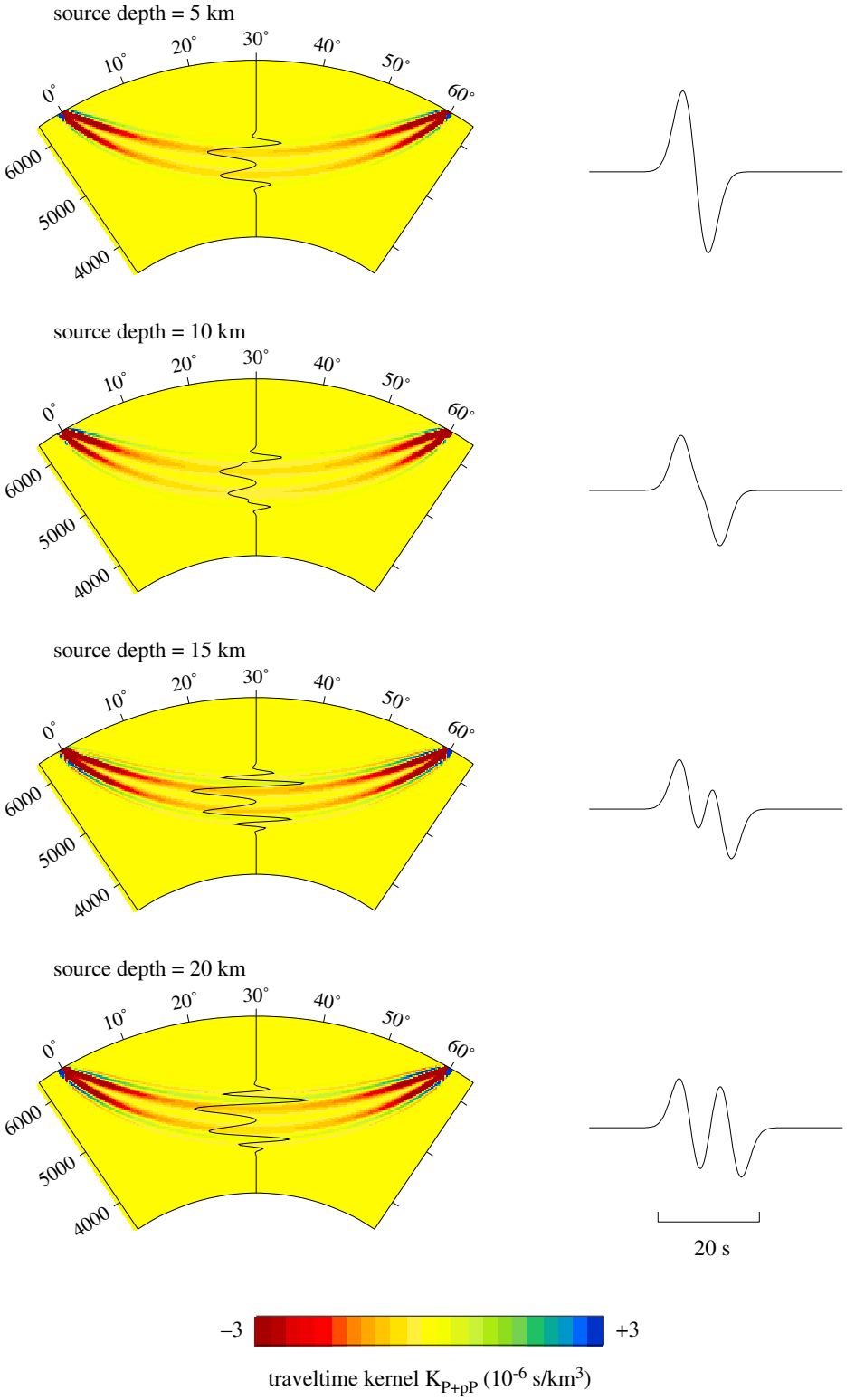

Figure 19. (Left) Ray-plane cross-sections of the paraxial Fréchet kernel for the overlapping direct and depth phase $P+pP$. The source depth d varies from 5 km (top) to 20 km (bottom); the characteristic period of the waves is $\tau=20$ s. (Right) Corresponding ray-theoretical waveforms $p_P(t)+p_{pP}(t)$.

ACKNOWLEDGMENTS

The pseudospectral waveform modelling has been performed on a cluster of SP2 machines at the San Diego Supercomputer Center (SDSC). Most figures have been plotted using GMT (Wessel & Smith 1995). Financial support for this work has been provided by the US National Foundation under grants EAR-9505677 and EAR-9725496.

REFERENCES

Aki, K. & Richards, P.G., 1980. *Quantitative Seismology,* Freeman, New York.

Aki, K., Christoffersson, A. & Husebye, E.S., 1977. Determination of the three-dimensional seismic structure of the lithosphere, *J. geophys. Res.,* **82,** 277–296.

Ben-Menahem, A. & Singh, S.J., 1981. *Seismic Waves and Sources,* Springer-Verlag, New York.

Cerjan, C., Kosloff, D., Kosloff, R. & Reshef, M., 1985. A non-reflecting boundary condition for discrete acoustic and elastic wave equations, *Geophysics,* **50,** 705–708.

Dahlen, F.A. & Tromp, J., 1998. *Theoretical Global Seismology,* Princeton University Press, Princeton.

Dahlen, F.A., Hung, S.-H. & Nolet, G., 2000. Fréchet kernels for finite-frequency traveltimes—I. Theory, *Geophys. J. Int.,* **141,** 157–174 (this issue).

Grand, S.P., Van der Hilst, R.D. & Widiyantoro, S. 1997. Global seismic tomography: a snapshot of convection in the Earth, *GSA Today,* **7,** 1–7.

Gudmundsson, O., 1996. On the effect of diffraction on traveltime measurements, *Geophys. J. Int.,* **124,** 304–314.

Humphreys, E.D., Clayton, R.W. & Hager, B.H., 1984. A tomographic image of mantle structure beneath Southern California, *Geophys. Res. Lett.,* **11,** 625–627.

Hung, S.-H. & Forsyth, D.W., 1998. Modelling anisotropic wave propagation in oceanic inhomogeneous structures using the parallel multidomain pseudospectral method, *Geophys. J. Int.,* **133,** 726–740.

Katzman, R., Zhao, L. & Jordan, T.H., 1998. High resolution, 2-D vertical tomography of the central Pacific using ScS reverberations and frequency-dependent traveltimes, *J. geophys. Res.,* **103,** 17 933–17 971.

Kuo, B.-Y., Forsyth, D.W. & Wysession, M., 1987. Lateral heterogeneity and azimuthal anisotropy in the North Atlantic determined from SS-S differential traveltimes, *J. geophys. Res.,* **92,** 6421–6436.

Marquering, H., Dahlen, F.A. & Nolet, G., 1999. Three-dimensional sensitivity kernels for finite-frequency traveltimes: the banana–doughnut paradox, *Geophys. J. Int.,* **137,** 805–815.

Morse, P.M. & Ingard, K.U., 1968. *Theoretical Acoustics,* McGraw-Hill, New York.

Müller, G., Roth, M. & Korn, M., 1992. Seismic-wave traveltimes in random media, *Geophys. J. Int.,* **110,** 29–41.

Neele, F. & de Regt, H., 1999. Imaging upper-mantle discontinuity topography using underside-reflection data, *Geophys. Res. Lett.,* **137,** 91–106.

Neele, F. & Snieder, R., 1992. Topography of the 400 km discontinuity from observations of long-period P400P phases, *Geophys. J. Int.,* **109,** 670–682.

Neele, F., de Regt, H. & VanDecar, J., 1997. Gross errors in upper mantle discontinuity topography from P*d*P or S*d*S data, *Geophys. J. Int.,* **129,** 194–204.

Nolet, G. & Dahlen, F.A., 1999. Wavefront healing and the evolution of seismic delay times, *J. geophys. Res.,* submitted.

Nolet, G. & Moser, T.-J., 1993. Teleseismic delay times in a 3-D Earth and a new look at the S discrepancy, *Geophys. J. Int.,* **114,** 185–195.

Paulssen, H. & Stutzmann, E., 1996. On PP-P differential traveltime measurements, *Geophys. Res. Lett.,* **23,** 1833–1836.

Pilant, W.L., 1979. *Elastic Waves in the Earth,* Elsevier, Amsterdam.

Roth, M., Müller, G. & Snieder, R., 1993. Velocity shift in random media, *Geophys. J. Int.,* **115,** 552–563.

Shearer, P.M., Flanagan, M.P. & Hedlin, M.A.H., 1999. Experiments in migration processing of SS precursor data to image upper mantle discontinuity structure, *J. geophys. Res.,* **104,** 7229–7242.

Sheehan, A. & Solomon, S., 1991. Joint inversion of shear wave travel-time residuals and geoid and depth anomalies for long-wavelength variations in upper mantle temperature and composition along the Mid-Atlantic Ridge, *J. geophys. Res.,* **96,** 19 981–20 009.

Sipkin, S.A. & Jordan, T.H., 1976. Lateral heterogeneity of the upper mantle determined from the travel times of multiple ScS, *J. geophys. Res.,* **81,** 6307–6320.

Sipkin, S.A. & Jordan, T.H., 1980. Multiple ScS travel times in the western Pacific, implications for mantle heterogeneity, *J. geophys. Res.,* **85,** 853–861.

Sommerfeld, A., 1949. *Partial Differential Equations in Physics,* Academic Press, New York.

VanDecar, J. & Crosson, R., 1990. Determination of teleseismic relative phase arrival times using multi-channel cross-correlation and least squares, **80,** 150–159.

Vasco, D.W. & Majer, E.L., 1993. Wavepath traveltime tomography, *Geophys. J. Int.,* **115,** 1055–1069.

Wessel, P. & Smith, W.H.F., 1995. New version of the Generic Mapping Tools released, *EOS, Trans. Am. geophys. Un.,* **76,** Suppl., 329.

Wielandt, E., 1987. On the validity of the ray approximation for interpreting delay times, in *Seismic Tomography,* pp. 85–98, ed. Nolet, G., D. Reidel, Dordrecht.

Witte, O., Roth, M. & Müller, G., 1996. Ray tracing in random media, *Geophys. J. Int.,* **124,** 159–169.

Woodward, M.J., 1992. Wave-equation tomography, *Geophysics,* **57,** 15–26.

Woodward, R.L. & Masters, G., 1991. Global upper mantle structure from long-period differential traveltimes, *J. geophys. Res.,* **96,** 6351–6377.

Yomogida, K., 1992. Fresnel zone inversion for lateral heterogeneities in the Earth, *Pure appl. Geophys.,* **138,** 391–406.

Zhao, L. & Jordan, T.H., 1998. Sensitivity of frequency-dependent traveltimes to laterally heterogeneous, anisotropic Earth structure, *Geophys. J. Int.,* **133,** 683–704.

APPENDIX A: RAY TRACING IN A LINEAR-GRADIENT FLAT-EARTH MODEL

All of the spherical earth Fréchet kernels presented in this paper are for an acoustic model with a radial wave-speed variation of the form (48):

$$c(r) = (r/a)[c_0 + c' a \ln(a/r)] . \tag{A1}$$

This model was selected because of its convenient properties under the standard seismological earth-flattening transformation (Aki & Richards 1980):

$$z = a \ln(a/r) , \qquad c_{\rm flat}(z) = (a/r) c(r) . \tag{A2}$$

In fact, the flat-earth equivalent of (A1) is a *linear-gradient model*:

$$c_{\rm flat}(z) = c_0 + c' z . \tag{A3}$$

The quantity c_0 is the wave speed at the rigid upper surface $z = 0$, whereas $c' > 0$ is the rate of increase with depth z. We simulate the presence of a core–mantle boundary by terminating the linear profile (A3) with a second rigid surface at a depth $Z = a \ln(a/b)$. To compute and display a spherical earth kernel $K(r, \theta, \phi)$, we situate the source **s** and receiver **r** upon the equator $\theta = \pi/2$, as illustrated in Fig. 11, conduct all of the necessary ray tracing in the flat earth (A3), and then transform $K_{\rm flat}(x, y, z)$ via the reverse of (A2):

$$r = a \exp(-z/a) , \qquad \theta = y/a , \qquad \phi = x/(a \sin\theta) . \tag{A4}$$

We summarize the analytical details of our kinematic and dynamic ray-tracing procedures in this Appendix. Since all of the considerations that follow pertain to the flat earth, we shall henceforth drop the identifying label in (A3), setting $c_{\rm flat}(z) \rightarrow c(z)$ for simplicity. One aspect of our notation is worth

mentioning at the outset: the position of an arbitrary point is specified, as above, in terms of its three Cartesian coordinates, $\mathbf{x}=(x, y, z)$; points lying in the source–receiver plane will be distinguished by Greek letters, $\boldsymbol{\xi}=(\xi, 0, \zeta)$.

A1 Ray geometry

As is well known, every ray in a linear-gradient flat-earth model $c(z)=c_0+c'z$ is a *segment of a circle* (see e.g. Pilant 1979; Ben-Menahem & Singh 1981). An example of such a circular ray between two points,

$$\mathbf{x}_1=(\xi_1, 0, \zeta_1) \quad \text{and} \quad \mathbf{x}_2=(\xi_2, 0, \zeta_2)\,, \tag{A5}$$

is depicted in Fig. A1. The angles of incidence, measured clockwise from vertical, at the two endpoints are i_1 and i_2, respectively. The incidence angle of the circular extension of the ray at the surface $z=0$ is $\pi/2\le i_0\le\pi$, as shown. The height of the centre of the circle above the surface is

$$h=c_0/c'\,, \tag{A6}$$

and its radius is $R=h/\sin i_0$.

The traveltime of a direct wave between the two endpoints (A5) is

$$T=\int_{\mathbf{x}_1}^{\mathbf{x}_2}\frac{dl}{c}=-\frac{1}{c'}\int_{i_1}^{i_2}\frac{di}{\sin i}\,, \tag{A7}$$

where we have used the constancy of the ray parameter $p=\sin i/c$ to change the variable of integration from the arclength l to the local angle of incidence i. The integral in (A7) is elementary; the resulting traveltime is obviously independent of the direction of propagation:

$$T_{21}=T_{12}=\frac{1}{c'}\ln\left(\frac{\tan\frac{1}{2}i_2}{\tan\frac{1}{2}i_1}\right). \tag{A8}$$

The geometrical spreading factor $\mathscr{R}$ relates the differential cross-sectional area $d\Sigma$ of an infinitesimal ray tube to the subtended solid angle $d\Omega$ at its take-off point (Aki & Richards 1980; Dahlen & Tromp 1998, Sections 12.1.7 and 15.4.5):

$$\mathscr{R}=\sqrt{\frac{|d\Sigma|}{d\Omega}}\,. \tag{A9}$$

The $\mathbf{x}_1$-to-$\mathbf{x}_2$ and $\mathbf{x}_2$-to-$\mathbf{x}_1$ spreading factors in any plane-layered flat earth model are given by (Pilant 1979; Ben-Menahem & Singh 1981)

$$\mathscr{R}_{21}=\sqrt{\frac{|\xi_2-\xi_1|\,|\cos i_2|\,|\partial\xi_2/\partial i_1|_{\zeta_2}}{\sin i_1}}, \tag{A10}$$

$$\mathscr{R}_{12}=\sqrt{\frac{|\xi_1-\xi_2|\,|\cos i_1|\,|\partial\xi_1/\partial i_2|_{\zeta_1}}{\sin i_2}}, \tag{A11}$$

where the subscripts indicate that the partial derivatives $\partial\xi_2/\partial i_1$ and $\partial\xi_1/\partial i_2$ are measured along the ray-plane horizontals $\zeta=\zeta_2$ at $\mathbf{x}_2$ and $\zeta=\zeta_1$ at $\mathbf{x}_1$, respectively. The two spreading factors (A10)–(A11) are related by a dynamical symmetry relation (Aki & Richards 1980; Dahlen & Tromp 1998, Sections 12.1.7.and 15.4.6):

$$c_1\mathscr{R}_{21}=c_2\mathscr{R}_{12}\,. \tag{A12}$$

As noted, eq. (A8) gives the traveltime $T_{21}=T_{12}$ of a *direct wave*, with no boundary reflections between $\mathbf{x}_1$ and $\mathbf{x}_2$; the relations (A10)–(A12) are, in contrast, valid for all waves, including multiple reflections.

Tracing forward rays′ and backward rays″ from a source $\mathbf{s}$ and receiver $\mathbf{r}$ to an arbitrary scatterer $\mathbf{x}$ is a relatively straightforward matter based upon (A8) and (A10)–(A12). Multiple-bounce ray paths can be treated by patching together a series of circular arcs, requiring that Snell's law $[\sin i/c]_-^+=0$ be satisfied at every boundary. We summarize the results for a variety of ray paths in the sections that follow, restricting attention to a surface source and receiver:

$$\mathbf{s}=(0, 0, 0)\,, \qquad \mathbf{r}=(X, 0, 0)\,, \qquad \mathbf{x}=(x, y, z)\,, \tag{A13}$$

where $X=a\Delta$ is the flat-earth epicentral distance, and where the location of the scatterer is arbitrary. The procedure in every case is to first find an explicit or implicit relation between the

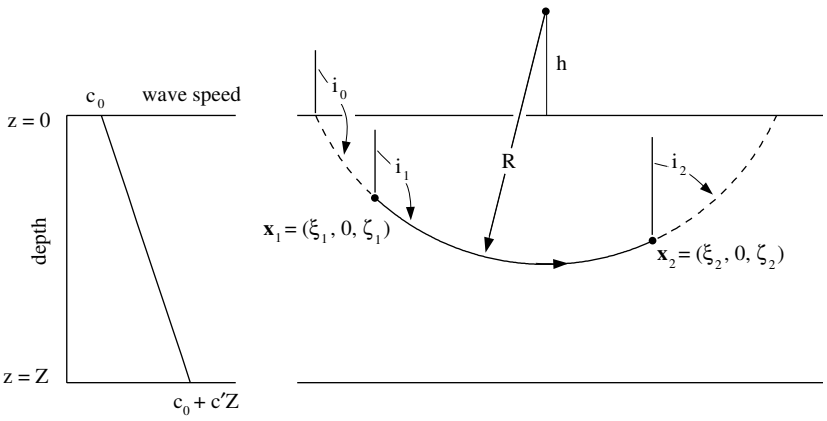

Figure A1. (Left) Flat-earth model with a constant-gradient wave speed $c(z)=c_0+c'z$ in the depth interval $0\le z\le Z$. (Right) Every direct ray between two points $\xi_1=(\xi_1, 0, \zeta_1)$ and $\xi_2=(\xi_2, 0, \zeta_2)$ within such an earth model is a segment of a circle. The height h of the centre above the surface and the radius R are defined in the text.

take-off incidence angle and the horizontal distance of propagation, enabling the partial derivatives in eqs (A10)–(A11) to be analytically evaluated. We omit all derivations, since they are uninteresting.

A2 *P* wave

We begin by considering the simplest case—a direct *P* wave with no surface reflections. The associated ray paths are depicted in Fig. A2.

A2.1 Source to receiver

The take-off incidence angle i_0 of the direct ray from the source $\mathbf{s}=(0, 0, 0)$ to the receiver $\mathbf{r}=(X, 0, 0)$ is given by

$$\tan i_0 = -2h/X\,. \tag{A14}$$

Since the ray leaves the source going down, it must be in the range $\pi/2 \le i_0 \le \pi$; the arrival angle at the receiver is $\pi - i_0$. The traveltime $T = T_{\rm rs}$, geometrical spreading factor $\mathscr{R} = \mathscr{R}_{\rm rs}$ and Maslov index $M = M_{\rm rs}$ are given by

$$T = \frac{2}{c'} \ln\left(\tan\frac{1}{2} i_0\right), \tag{A15}$$

$$\mathscr{R} = \frac{X}{\sin i_0}\,, \tag{A16}$$

$$M = 0\,. \tag{A17}$$

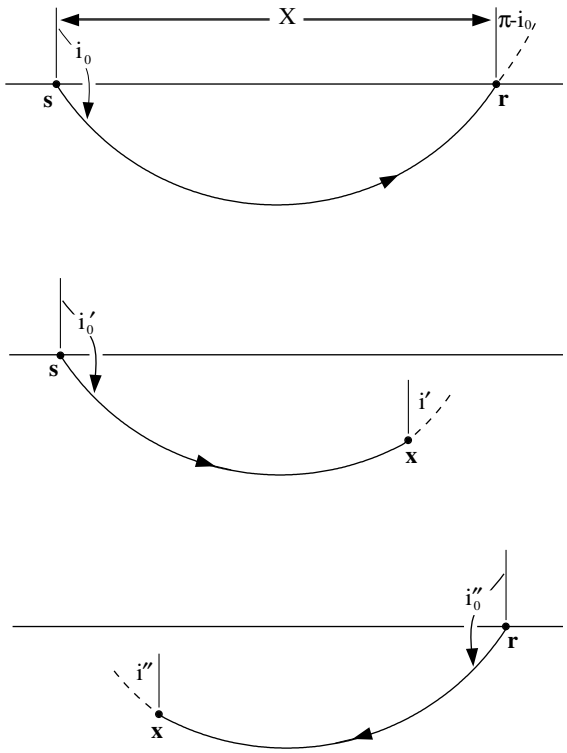

Figure A2. (Top) Direct *P* ray between a surface source **s** and receiver **r** showing the take-off and arrival angles i_0 and $\pi - i_0$. (Middle) Direct *P* ray′ from the source **s** to an arbitrary scatterer $\mathbf{x}=(x, y, z)$. (Bottom) Backward *P* ray″ from the receiver **r** to a scatterer **x**. The incidence angles i_0', i' and i_0'', i'' are measured in the vertical planes through **s** and **x** and through **r** and **x**, respectively; whenever $y \neq 0$, these planes will not coincide with either the source–receiver ray plane or each other.

A2.2 Source to scatterer

The take-off angle $\pi/2 \le i_0' \le \pi$ of the direct ray′ from the source $\mathbf{s}=(0, 0, 0)$ to an arbitrary off-plane scatterer $\mathbf{x}=(x, y, z)$ is given by

$$\tan i_0' = -\frac{2h\sqrt{x^2+y^2}}{x^2+y^2+z(z+2h)}\,. \tag{A18}$$

The arrival angle i' of the ray′ at the scatterer is related to the take-off angle i_0' by

$$\frac{\cos i'}{\cos i_0'} = \frac{z(z+2h)-x^2-y^2}{z(z+2h)+x^2+y^2}\,. \tag{A19}$$

The incoming ray′ at **x** arrives from above ($\pi/2 \le i' \le \pi$) or below ($0 \le i' \le \pi/2$) depending upon whether it is above or below the hyperboloid $z(z+2h)-x^2-y^2=0$. The source-to-scatterer traveltime $T' = T_{\rm xs}$, geometrical spreading factor $\mathscr{R}' = \mathscr{R}_{\rm xs}$ and Maslov index $M' = M_{\rm xs}$ are given by

$$T' = \frac{1}{c'} \ln\left(\frac{\tan\frac{1}{2} i_0'}{\tan\frac{1}{2} i'}\right), \tag{A20}$$

$$\mathscr{R}' = \frac{\sqrt{x^2+y^2}}{\sin i_0'}\,, \tag{A21}$$

$$M' = 0\,. \tag{A22}$$

A2.3 Receiver to scatterer

The ray″ from the receiver $\mathbf{r}=(X, 0, 0)$ to the scatterer $\mathbf{x}=(x, y, z)$ can be traced by simply altering the horizontal propagation distance:

$$\sqrt{x^2+y^2} \to \sqrt{(X-x)^2+y^2}\,. \tag{A23}$$

The backward take-off angle i_0'', arrival angle i'', traveltime $T'' = T_{\rm xr}$, spreading factor $\mathscr{R}'' = \mathscr{R}_{\rm xr}$ and Maslov index $M'' = M_{\rm xr}$ are given by the analogues of (A18)–(A22):

$$\tan i_0'' = -\frac{2h\sqrt{(X-x)^2+y^2}}{(X-x)^2+y^2+z(z+2h)}\,, \tag{A24}$$

$$\frac{\cos i''}{\cos i_0''} = \frac{z(z+2h)-(X-x)^2-y^2}{z(z+2h)+(X-x)^2+y^2}\,, \tag{A25}$$

$$T'' = \frac{1}{c'} \ln\left(\frac{\tan\frac{1}{2} i_0''}{\tan\frac{1}{2} i''}\right), \tag{A26}$$

$$\mathscr{R}'' = \frac{\sqrt{(X-x)^2+y^2}}{\sin i_0''}\,, \tag{A27}$$

$$M'' = 0\,. \tag{A28}$$

A3 *PP* wave

A *PP* wave having a single underside reflection off the upper surface $z=0$ is the next most complicated case. The ray paths of interest are sketched in Fig. A3.

A3.1 Source to receiver

This is simply a concatenation of two identical rays, each of which traverses a horizontal distance $X/2$. It is well known that such a *PP* surface reflection is a minimax phase, having passed through a single caustic on its second leg; the take-off angle, traveltime, geometrical spreading factor and Maslov index are given by

$$\tan i_0 = -4h/X\,, \tag{A29}$$

$$T = \frac{4'}{c}\ln\left(\tan\frac{1}{2}\,i_0\right), \tag{A30}$$

$$\mathscr{R} = \frac{X}{\sin i_0}\,, \tag{A31}$$

$$M = 1\,. \tag{A32}$$

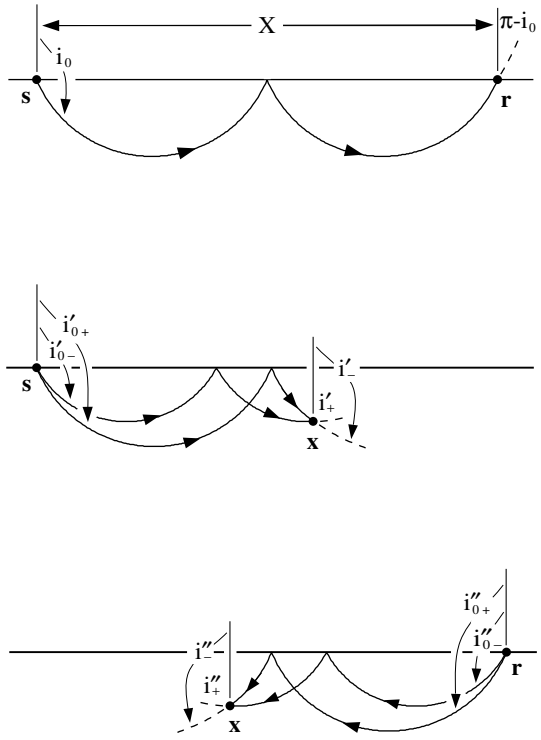

Figure A3. (Top) One-bounce *PP* ray between a surface source **s** and receiver **r**. The surface reflection occurs at the midpoint, $\mathbf{x}_b=(X/2, 0, 0)$. (Middle) Two *PP* rays′ can propagate between a surface source **s** and an arbitrary scatterer **x**. The shallower of these, with take-off angle i_{0-} and arrival angle i'_-, has passed through the *PP* caustic $x^2+y^2-8z(z+2h)=0$ on its second leg before arriving at **x**, and has $M'=1$, whereas the steeper one, with take-off angle i_{0+} and arrival angle i'_+, has not yet passed through the caustic, and has $M'=0$. The two rays′ merge and arrive with a downward incidence angle, given by $\cos i' = \cos i'_0/3$ in the case of a scatterer *on* the caustic. The $\pm$ labels in the above discussion are the same as those in eqs (A33)–(A34). (Bottom) There are likewise two backward *PP* rays″, with take-off angles $i''_{0\pm}$ and arrival angles $i''_\pm$, from the receiver **r** to an arbitrary scatterer **x**. The receiver-to-source caustic is given by $(X-x)^2+y^2-8z(z+2h)=0$.

A3.2 Source or receiver to scatterer

Two single-bounce *PP* waves can propagate from a surface source $\mathbf{s}=(0, 0, 0)$ to an arbitrary scatterer $\mathbf{x}=(x, y, z)$. Their take-off angles at the source and arrival angles at the receiver are given by

$$\tan i'_0 = \frac{-3h\sqrt{x^2+y^2} \pm h\sqrt{x^2+y^2-8z(z+2h)}}{x^2+y^2+z(z+2h)}\,, \tag{A33}$$

$$\frac{\cos i'}{\cos i'_0} = \frac{3z(z+2h) \pm \sqrt{x^2+y^2}\sqrt{x^2+y^2-8z(z+2h)}}{x^2+y^2+z(z+2h)}\,. \tag{A34}$$

The traveltimes $T'=T_{xs}$ and spreading factors $\mathscr{R}'=\mathscr{R}_{xs}$ of these waves are

$$T' = \frac{2}{c'}\ln\left(\tan\frac{1}{2}\,i'_0\right) + \frac{1}{c'}\ln\left(\frac{\tan\frac{1}{2}\,i'_0}{\tan\frac{1}{2}\,i'}\right), \tag{A35}$$

$$\mathscr{R}' = \frac{\sqrt{x^2+y^2}}{\sin i'_0}\left|\frac{\cos i'/\cos i'_0 - \frac{1}{3}}{\frac{1}{3}\cos i'/\cos i'_0 - 1}\right|^{1/2}. \tag{A36}$$

The hyperboloid $x^2+y^2-8z(z+2h)=0$ is the caustic or envelope of *PP* rays′. The $\pm$ signs in (A33) and (A34) distinguish rays′ that either have not or have passed through the caustic before arriving at **x**. Passage through the caustic gives rise to a non-geometrical $\pi/2$ phase shift; the Maslov index $M'=M_{xs}$ is given by

$$M' = \begin{cases} 0 & \text{if } + \text{in eqs (A33)–(A34)} \\ 1 & \text{if } - \text{in eqs (A33)–(A34)} \end{cases}. \tag{A37}$$

The spreading factor vanishes, $\mathscr{R}'\to 0$, for a scatterer **x** situated *on* the caustic hyperboloid, where the $\pm$rays′ cross; the common arrival angle at this point of tangency is given by $\cos i' = \cos i'_0/3$. To find the angles i''_0, i'', traveltimes T'', spreading factors $\mathscr{R}''$ and Maslov indices M'' along the $\pm$ backward rays″ from the receiver $\mathbf{r}=(X, 0, 0)$, we again employ the substitution (A23).

A4 *PcP* wave

Finally, we consider the case of a *PcP* wave reflected once off the core–mantle boundary at $z=Z$, as illustrated in Fig. A4.

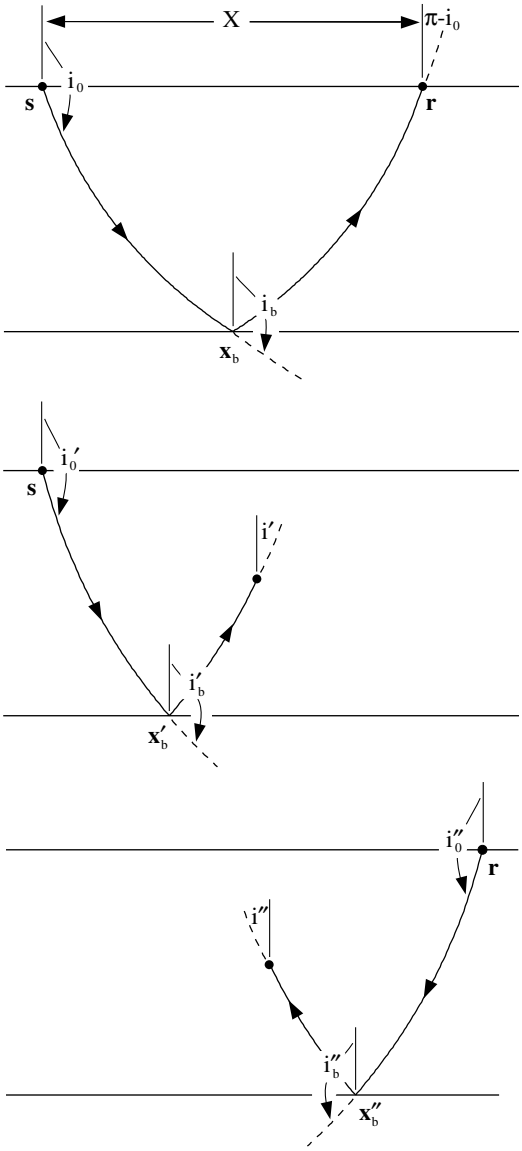

Figure A4. (Top) *PcP* ray between a surface source **s** and receiver **r** showing the take-off and arrival angles i_0 and $\pi - i_0$ and the incidence angle i_b upon reflection off the core–mantle boundary at $\mathbf{x}_b = (X/2, 0, Z)$. (Middle) Forward *PcP* ray′ with one core–mantle boundary reflection between the source **s** and an arbitrary scatterer $\mathbf{x} = (x, y, z)$. (Bottom) Backward *PcP* ray″ between the receiver **s** and **x**.

A4.1 Source to receiver

The take-off angle $\pi/2 \le i_0 \le \pi$ of a *PcP* ray at the source $\mathbf{s} = (0, 0, 0)$ and the arrival angle $\pi/2 \le i_b \le \pi$ at the bounce point $\mathbf{x}_b = (X/2, 0, Z)$ are given by

$$\tan i_0 = -\frac{4hX}{X^2 + 4Z(Z+2h)}, \tag{A38}$$

$$\frac{\cos i_b}{\cos i_0} = \frac{4Z(Z+2h) - X^2}{4Z(Z+2h) + X^2}. \tag{A39}$$

The source-to-receiver traveltime $T = T_{rs}$, spreading factor $\mathscr{R} = \mathscr{R}_{rs}$ and Maslov index $M = M_{rs}$ are

$$T = \frac{2}{c'} \ln\left(\frac{\tan\frac{1}{2} i_0}{\tan\frac{1}{2} i_b}\right), \tag{A40}$$

$$\mathscr{R} = \frac{X}{\sin i_0} \sqrt{\frac{\cos i_0}{\cos i_b}}, \tag{A41}$$

$$M = 0. \tag{A42}$$

A4.2 Source or receiver to scatterer

The take-off angle $\pi/2 \le i'_0 \le \pi$ of the ray′ from $\mathbf{s} = (0, 0, 0)$ to an arbitrary scatterer $\mathbf{x} = (x, y, z)$ satisfies

$$\sqrt{x^2+y^2}\tan i'_0 + h + \sqrt{h^2 - z(z+2h)\tan^2 i'_0} - 2\sqrt{h^2 - Z(Z+2h)\tan^2 i'_0} = 0. \tag{A43}$$

In every case considered so far, i_0, i'_0 or i''_0 can be found explicitly with an arctan call. Eq. (A43) is, in contrast, a genuinely implicit relation; this is the first instance in which a numerical root finder must be used to solve the two-point ray-tracing problem. Once i'_0 has been found, the down-going incidence angle i'_b at the core–mantle boundary bounce point and the upgoing incidence angle i' at the scatterer are determined by

$$\frac{\cos i'_b}{\cos i'_0} = \frac{1}{h}\sqrt{h^2 - Z(Z+2h)\tan^2 i'_0}, \tag{A44}$$

$$\frac{\cos i'}{\cos i'_0} = -\frac{1}{h}\sqrt{h^2 - z(z+2h)\tan^2 i'_0}. \tag{A45}$$

The traveltime $T' = T_{xs}$, spreading factor $\mathscr{R}' = \mathscr{R}_{xs}$ and Maslov index $M' = M_{xs}$ are given by

$$T' = \frac{1}{c'} \ln\left(\frac{\tan\frac{1}{2} i'_0}{\tan\frac{1}{2} i' \tan^2\frac{1}{2} i'_b}\right), \tag{A46}$$

$$\mathscr{R}' = \left|\frac{\sqrt{x^2+y^2}\cos i'}{\sin i'_0 \cos^2 i'_0}\right|^{1/2} \left|\frac{2Z(Z+2h)}{\sqrt{h^2 - Z(Z+2h)\tan^2 i'_0}} - \frac{z(z+2h)}{\sqrt{h^2 - z(z+2h)\tan^2 i'_0}} + \frac{\sqrt{x^2+y^2}}{\tan i'_0}\right|^{1/2}, \tag{A47}$$

$$M' = 0. \tag{A48}$$

The quantities i''_0, i''_b, i'', T'', $\mathscr{R}''$ and M'' along the backward ray″ from $\mathbf{r} = (X, 0, 0)$ may be found in an analogous manner, using the substitution (A23).

A5 Traveltime Hessian

The paraxial Fréchet kernel (27)–(28) is completely specified in terms of the forward and backward traveltime Hessians $\mathbf{M}' = \mathbf{M}_{\xi s}$ and $\mathbf{M}'' = \mathbf{M}_{\xi r}$. In this section, we present explicit expressions for these 2×2 matrices, as a function of the horizontal distance $0 \le \xi \le X$ from the source.

A5.1 P wave

The Hessians for a *P* wave from a surface source $\mathbf{s}=(0,0,0)$ to a receiver $\mathbf{r}=(X,0,0)$ are

$$\mathbf{M}'=\frac{\sin i_0}{c_0}\begin{pmatrix}\frac{1}{\xi} & 0\\ 0 & \frac{1}{\xi}\end{pmatrix}, \tag{A49}$$

$$\mathbf{M}''=\frac{\sin i_0}{c_0}\begin{pmatrix}\frac{1}{X-\xi} & 0\\ 0 & \frac{1}{X-\xi}\end{pmatrix}. \tag{A50}$$

A5.2 PP wave

In the case of a minimax *PP* wave between $\mathbf{s}=(0,0,0)$ and $\mathbf{r}=(X,0,0)$, the Hessians are

$$\mathbf{M}'=\begin{cases}\dfrac{\sin i_0}{c_0}\begin{pmatrix}\frac{1}{\xi} & 0\\ 0 & \frac{1}{\xi}\end{pmatrix} & \text{if } 0\le\xi<\frac{1}{2}X\\[2ex] \dfrac{\sin i_0}{c_0}\begin{pmatrix}\frac{1}{\xi-\frac{2}{3}X} & 0\\ 0 & \frac{1}{\xi}\end{pmatrix} & \text{if } \frac{1}{2}X<\xi\le X\end{cases}, \tag{A51}$$

$$\mathbf{M}''=\begin{cases}\dfrac{\sin i_0}{c_0}\begin{pmatrix}\frac{1}{\frac{1}{3}X-\xi} & 0\\ 0 & \frac{1}{X-\xi}\end{pmatrix} & \text{if } 0\le\xi<\frac{1}{2}X\\[2ex] \dfrac{\sin i_0}{c_0}\begin{pmatrix}\frac{1}{X-\xi} & 0\\ 0 & \frac{1}{X-\xi}\end{pmatrix} & \text{if } \frac{1}{2}X<\xi\le X\end{cases}. \tag{A52}$$

Both $\mathbf{M}'$ and $\mathbf{M}''$ exhibit jump discontinuities at the surface reflection point $\xi_b=X/2$; nevertheless, their sum is continuous: $[\mathbf{M}'+\mathbf{M}'']^+_-=\mathbf{0}$. The source-to-receiver and receiver-to-source waves pass through caustics on their second legs, at $\xi=2X/3$ and $\xi=X/3$, respectively. The $(\xi-2X/3)^{-1}$ divergence of $\mathbf{M}'$ and the $(X/3-\xi)^{-1}$ divergence of $\mathbf{M}''$ reflect the pinching off of the ray tube at these two points. The jumps $2\to0\to2$ in the signature of $\mathbf{M}'+\mathbf{M}''$ at $\xi=X/3$ and $\xi=2X/3$ are responsible for one of the most characteristic features of the *PP* kernel: the sensitivity is identically zero along the geometrical ray between the source and the receiver-to-source caustic, $0\le\xi<X/3$, and between the receiver and the source-to-receiver caustic, $2X/3<\xi\le X$, whereas it is maximal along the ray in the region between the two caustics, $X/3<\xi<2X/3$.

A5.3 PcP wave

Finally, the Hessians for a *PcP* wave between $\mathbf{s}=(0,0,0)$ and $\mathbf{r}=(X,0,0)$ are

$$\mathbf{M}'=\begin{cases}\dfrac{\sin i_0}{c_0}\begin{pmatrix}\frac{1}{\xi} & 0\\ 0 & \frac{1}{\xi}\end{pmatrix} & \text{if } 0\le\xi<\frac{1}{2}X\\[2ex] \dfrac{\sin i_0}{c_0}\begin{pmatrix}\frac{A}{\frac{1}{2}X+A\left(\xi-\frac{1}{2}X\right)} & 0\\ 0 & \frac{1}{\xi}\end{pmatrix} & \text{if } \frac{1}{2}X<\xi\le X\end{cases}, \tag{A53}$$

$$\mathbf{M}''=\begin{cases}\dfrac{\sin i_0}{c_0}\begin{pmatrix}\frac{A}{\frac{1}{2}X-A\left(\xi-\frac{1}{2}X\right)} & 0\\ 0 & \frac{1}{X-\xi}\end{pmatrix} & \text{if } 0\le\xi<\frac{1}{2}X\\[2ex] \dfrac{\sin i_0}{c_0}\begin{pmatrix}\frac{1}{X-\xi} & 0\\ 0 & \frac{1}{X-\xi}\end{pmatrix} & \text{if } \frac{1}{2}X<\xi\le X\end{cases}, \tag{A54}$$

where

$$A=\frac{Z(Z+2h)+\frac{3}{4}X^2}{Z(Z+2h)-\frac{1}{4}X^2}. \tag{A55}$$

A6 More complicated cases

A similar circular-arc-patching method may be used to trace rays that are reflected more than once off either or both the upper surface or the core–mantle boundary, as well as rays that leave from a buried rather than a surface source. In all cases, the kinematic and dynamical quantities of interest—the traveltimes T, T', T'', geometrical spreading factors $\mathscr{R}$, $\mathscr{R}'$, $\mathscr{R}''$, Maslov indices M, M', M'' and ray-plane Hessians $\mathbf{M}'$, $\mathbf{M}''$—may be determined either entirely or almost entirely analytically. The algebraic details are somewhat but not a great deal more complicated than those given above.